Computational methods enable hybrid dynamical systems applications in cancer research

Awoyemi, Boluwatife[1] Young, Robert S.[1,2] Vigil, Bradley Z.[1] Sah, Naresh[3]
Thompson, Travis B.[1] Almodovar, Sharilyn[2,†] Laubmeier, Amanda[1,†,*]

[1] Department of Mathematics and Statistics,
Texas Tech University, Lubbock, Texas
[2] Department of Immunology and Molecular Microbiology,
Texas Tech Health Sciences Center, Lubbock, Texas
[3] Department of Cell Biology and Biochemistry,
Texas Tech Health Sciences Center, Lubbock, Texas

[†] Senior author
[*]Corresponding author: Amanda.Laubmeier@ttu.edu

March 10, 2026

Abstract

Keywords: Computational stability analysis, Hybrid modeling, Equilibrium analysis, Cancer treatment, Statistical Machine Learning.

1 Introduction

Mathematical models of physical processes make use of time-varying equations based on foundational mechanisms. The time variable is most often treated either continuously (differential equations) or discretely (difference equations). A number of important and practical problems, especially in ecology and biomedicine, conjoin mechanisms at both scales.

Hybrid dynamical system models [9, 22, 24, 32, 35] consist of at least one continuous-time equation coupled to at least one discrete time equation. Hybrid models are a direct template for the cross-disciplinary study of a panoply of applied problems with translational applications to human pathophysiology being particularly well suited to this regime. A significant drawback of these models is the relatively intractable analysis, outside of simpler paradigms [32], of their behavior and their mathematical stability. Given the potential of hybrid models to address significant problems across biology and biomedicine, these types of model systems should be further developed theoretically and informed by experiment to facilitate testable predictions in real-world settings. In this manuscript, our goal is two fold: first, to demonstrate how hybrid models may be used, alongside experimental data, in biomedical practice; and second, to demonstrate that a computational analysis of model dynamics is useful for applied scientists, at least until analytic techniques can be developed for wider classes of hybrid problems.

The use of conventional techniques to model both homo- and heterogeneous cancer cell population dynamics is a well-established area of research. Examples include continuous time dynamical systems models of interactions between effector cells and immunogenic tumor cells [2, 6, 26], tumor response to immunotherapy [3] or treatment regimes defined by either continuous dosing schedules [13] or by determining dosing schedules through optimization methods [8, 30]. Traditional techniques have also been used to study attributes of heterogeneous cancer cell populations, such as: how treatment resistance may arise due either to existing resistant cells [4, 5, 7] or as an adaptive response to drug exposure [15, 21]; and how treatment regimes [15], cellular facilitation or competition [23, 27, 37] and genetic shifts [31] may drive coexistence, exclusion, or dominance of resistant cells. Despite these advances, traditional modeling methods remain limited in their ability to represent the discontinuous nature of chemotherapeutic treatments in clinical practice.

Chemotherapeutic treatment is an ideal illustration of the portents of hybrid models to translational practice. Within heterogeneous cancer cell populations, rapid growth and competition reflect continuous-time dynamics, while chemotherapeutic intervention is a discrete phenomenon with differential implications to cell quantity and cell dynamics for resistive versus susceptible cells. Hybrid continuous-discrete time models naturally address this gap [12, 17, 24, 29] by capturing both the smooth proliferation of cancer cells and the abrupt cytotoxic effects of various, realistic treatment cycle protocols. Discrete pulses can alter the structure of continuous dynamical systems, an observation that may be highly important in practice but significantly complexifies, or all together obviates, traditional analytic techniques, which often yield only partial insights into the behavior of hybrid systems. In this manuscript we demonstrate, for the discerning practitioner concerned primarily with applications, that the behavior and stability of hybrid systems can be well-investigated computationally. To do so, we modify the model from Luo, *et al.* [29], in which a comprehensive analysis of dynamics is not presented, 2-species model of resistant and susceptible cell grown and competition in the presence of discrete chemotherapeutic

intervention. The continuous model is parameterized using statistical machine learning applied to in vitro, homogeneous, SKOV3 (treatment susceptible) and CP20 (treatment resistant) ovarian cancer cell count assays; discrete treatment effects are partially parameterized by Somasagara, *et al.* [16] and partially by our machine learning results. We demonstrate the analysis of competition and treatment effects on cell population persistence and stability using our methodology described, in full, in [35]. In doing so, we demonstrate that hybrid models may be used alongside in vitro experimental data and that computational methods can effectively analyze these systems, thereby closing a significant gap in biological and biomedical research, at least until new mathematical approaches can be developed.

2 Methods

2.1 Experiment & Image Acquisition

Table 1: Cell culture experimental details for carboplatin-resistant (A2780/CP20) and carboplatin-susceptible (SKOV3) human ovarian cancer cell lines. Cells were treated with vehicle control (Control cells) or with 14μM carboplatin (Treated cells). After application of vehicle/carboplatin, cell counts were assessed every two hours by live cell analysis of automatic image segmentation.

Experimental Regime	Approx. Initial Confluence	Number of well cultures
CP20 Control	20%	11
CP20 14μM Treated	20%	11
SKOV3 Control	20%	10
SKOV3 14μM Treated	20%	9

The human ovarian cancer cell line SKOV3 used in our experiment was obtained from the American Type Culture Collection (ATCC). The carboplatin-resistant cell line A2780-CP20 is a derivative of SKOV3, which was generated by intermittent carboplatin exposure while routinely maintained under continuous carboplatin selection in culture. This derivative carboplatin resistance of SKOV3/CP20 relative to parental SKOV3 has been previously validated by clonogenic survival and increased carboplatin tolerance [16]. Both cell lines were provided by the Palle lab at Texas Tech University Health Sciences Center (TTUHSC), where they were routinely tested for mycoplasma and authenticated per standard laboratory practice.

The SKOV3 and CP20 cell lines were cultured using serum-containing Dulbecco's Modified Eagle Medium (DMEM) and 1:1 DMEM/F12, respectively. The day prior to imaging, cells were seeded at an estimated twenty percent initial confluence, approximately

2000 cells in 0.32 cm^2 in 96-well plates (Nunc). Cells were then incubated overnight at 37 degrees Celsius and 5 percent CO^2, for 24 hours to allow for adherence. Prior to imaging, the media were removed and replaced with DMEM or DMEM/F12 with the designated concentration of carboplatin or vehicle control (DMSO). Subsequently, cells were incubated in the CellCyte X in identical culture conditions for 72 hours. Using a 4X objective in phase contrast mode, whole-well images were acquired at 2-hour intervals in the Almodovar lab, at the TTUHSC (Table 1). Images were acquired and segmented using the CellCyte X and the Cytena CellCyte X analysis software. The exact specifications for the image mask can be accessed upon request. Segmented images were analyzed to quantify percent confluence and generate cell growth curves.

2.2 Hierarchical Bayesian parameter inference from cell quantification data

Well-cultured cells have a limited growth medium. Following an initial proliferation phase, the per capita population growth rate will attenuate, due to excessive cell growth, depletion of nutrients in the media, which results in a plateau in the overall cell population count (Figure 1). with eventual cell starvation and death. This type of population-limiting dynamic has also been recognized in paragangliomas of the head and neck [18].

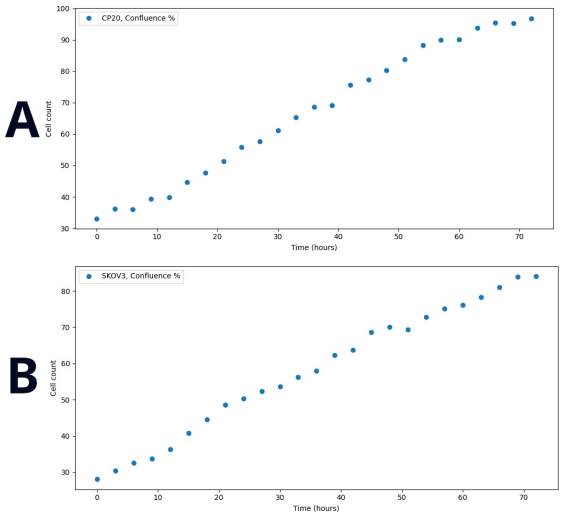

Figure 1: Confluence time series data recorded from the Cytena CellCyte X analysis software. (A) CP20 and (B) SKOV3; confluence percentage (y-axis) versus hours (x-axis).

Ovarian cancer cell line (CP20, SKOV3) percentage confluence data were tabulated, with 2-hour imaging periodicity, over 72 hours; the results were recorded as time-series data for further processing (Figure 1). In total, time series data from 11 trials were available for the CP20 control case and 11 were available for the 14μM CP20 carboplatin treatment case. For SKOV3, 10 time series trials were available for the control case while 9 trials were available for the 14μM SKOV3 carboplatin treatment case. To account for an initial expansion and pursuant plateau, a logistic equation, with parameters K, λ and P_0, was used to model cell confluence data as a function of time (Sections 2.3 and

3.1). Given the experimental confluence data, a hierarchical Bayesian model approach (Appendix B) was used to infer the posterior distributions of the model hyperparameters (Appendix B, Figure 12). To carry out the Bayesian parameter inference, an additive Gaussian error model, with noise parameter σ_E^2, was adopted; the Gaussian error model assumption produces a likelihood function defined by

$$P(X \mid \theta, \phi) \sim N\left(\mu = F(t;\theta,\phi), \sigma^2 = \sigma_E^2\right),$$

where X denotes the multi-well experimental, CP20 or SKOV3, control data, θ denotes the vector of mathematical (logistic) model parameters, ϕ is the vector of hierarchical hyperparameters and $F(t;\theta,\phi)$ is the data generated by the (logistical) mathematical growth model at time t and with the parameter choices determined by θ and ϕ. The prior distributions used in the model, for each parameter and hyperparameter, are listed in Table 2.

We used PyMC, a probabilistic Markov Chain Monte Carlo (MCMC) based programming library [25], to implement and to run the model inference. The inference model was run on an EPYC 44-core workstation with 512GB of DDR5 ram; 4 parallel chains were used with 4,500 burn-in and 5,000 posterior draws with a target accept rate of 0.99 using the No-U-Turn sampler (NUTS). Convergence of the chains, to the posterior distribution, was verified through R-hat values that coincided with 1.0, high essential bulk and essential tail counts and visual inspection of the inference traces. This procedure produced 20,000 posterior samples corresponding to each hyperparameter (mean and standard deviation) for each model parameter (Section 3.1).

Table 2: Prior distributions for the growth rate (λ), carrying capacity (K), initial value (P_0), measurement error σ_E^2, and hierarchical hyperparameters

Hyperparameter	Weakly informative hyperparameter priors, truncated normal distributions
λ_μ	$\mu = 0$, $\sigma = 10$, bounds: $0 \leq \lambda_\mu$
K_μ	$\mu = 0$, $\sigma = 100$, bounds: $0 \leq K_\mu \leq 100$
P_{0_μ}	$\mu = 0$, $\sigma = 30$, bounds: $0 \leq P_{0_\mu}$
λ_σ	$\mu = 1$, $\sigma = 5$, bounds:$0 \leq \lambda_\sigma$
K_σ	$\mu = 1$, $\sigma = 5$, bounds: $0 \leq K_\sigma$
P_{0_σ}	$\mu = 1.0$, $\sigma = 5$, bounds: $0 \leq P_{0_\sigma}$
Model parameter	Parameter priors, truncated normal distributions
λ	$\mu = \lambda_\mu$, $\sigma = \lambda_\sigma$, bounds: $0 \leq \lambda$
K	$\mu = K_\mu$, $\sigma = K_\sigma$, bounds: $0 \leq K \leq 100$
P_0	$\mu = P_{0_\mu}$, $\sigma = P_{0_\sigma}$, bounds: $0 \leq P_0$

2.3 Hybrid model and simulation

We modified the hybrid model from [29] to describe the dynamics of the cell subpopulations, drug-sensitive cells (S) and drug-resistant cells (R), with discrete-time treatment administrations. [29] models impulsive (discrete) dosage which reduces the sensitive cell population and increases resistant cells in discrete time, whereas, our model examines drug efficacy on both cells. This modeling technique follows from previous works [9, 22, 35]. The continuous part constitutes intrinsic post-surgery cell population growth in logistic manner with a limiting effect in the form of a competition term that arises from the presence of the other cell type. The continuous cycle runs for $T = 21$ days, so that the continuous timing is defined as $s = [0, T]$. Next, the discrete counterpart accounts for cell population after treatment administration by calculating the number of cells that survived treatment using drug efficacy rates from [16]. S and R are reduced based on the drug-efficacy rates, p and q respectively, at each treatment regimen time t. That is, S grows intrinsically at the rate λ_S in a logistic term $\lambda_S S\left(1-\frac{S}{K_S}\right)$ where K_S is the carrying capacity of sensitive cell population in the system. S also depletes at the rate $-\lambda_S S\left(\frac{a_{SR}R}{K_S}\right)$ due to the presence of R in the system, where λ_S represents the daily growth rate of S. The same process describes R population dynamics. Although the carrying capacity from fits to data describe the maximum percentage of cell density each experimental well can support, we interpret the carrying capacities K_S and K_R in our model as the tumor burden corresponding to the proliferation level of each cell subpopulation. That is, we maintain that a body has a maximum tumor volume which develops from the amount of dividing cells the resources available in the body can sustain before death.

$$\begin{aligned} \frac{dS}{ds} &= \lambda_S S\left(1-\frac{S+a_{SR}R}{K_S}\right), \quad S(0) = ST_t \\ \frac{dR}{ds} &= \lambda_R R\left(1-\frac{a_{RS}S+R}{K_R}\right), \quad R(0) = RT_t \end{aligned} \tag{1}$$

$$\begin{aligned} ST_{t+1} &= (1-p)S(T^-) \\ RT_{t+1} &= (1-q)R(T^-) \end{aligned} \tag{2}$$

Table 3: Description of parameters and variables used in the cancer cells equations (1) and (2), with values used in numerical results. Parameters marked with * were inferred from experimental data using Bayesian Inference (MCMC).

Parameter	Description	Values	Source
a_{SR}	Inter-specific competition effect of R on S	$a_{SR} \in [0.01, 2]$	-
λ_S (day^{-1})	Average S growth rate used in analysis	1.0807	Inferred*
K_S (%)	Average S carrying capacity used in analysis	99.7741	Inferred*
p	Drug effect on S	0.82	[16]
P	Drug effect on λ_S	0.0893	Inferred*
a_{RS}	Inter-specific competition effect of S on R	$a_{RS} \in [0.01, 2]$	-
λ_R (day^{-1})	Average R growth rate used in analysis	1.0924	Inferred*
K_R (%)	Average R carrying capacity used in analysis	99.7245	Inferred*
q	Drug effect on R	0.26	[16]
Q	Drug effect on λ_R	0.00	Inferred*
s (day)	Time between pulses	[0, 21]	[36]
t	Number of treatment cycles	9	[19, 36]

We map clinical Area Under Curve (AUC) in mg/mL to peak carboplatin concentration (C_{max}) using Pharmacokinetic data from [14] involving a lung cancer clinical trial where AUC = 6 and average $C_{max} = 22.6$ mg /mL. Using the molecular weight of carboplatin (≈ 371.254 g/mol), calculated C_{max} (22.6 mg /mL) $\approx 60.87\mu M$. When adjusted for early protein binding and the amount of drug that penetrates cells within early hours of drug administration (free drug $\approx 71\%$ of initial C_{max}), the drug concentration reduces to $\approx 43.22\mu M$. Therefore we utilize $40\mu M$ of free-drug carboplatin to parameterize in vitro treatment effect in the model even though the highest drug concentration used in our laboratory experiment was $14\mu M$. We extract these rates from [16] for cell lines used in our experimental study. We then generate results for nine chemotherapeutic treatment cycles which is the maximum one-course treatment regimen observed in real clinical trials [36] from UK's Medical Research Council (MRC), Gynecologic Oncology Group (GOG), etc.

For all simulations in the competition parameter space a_{SR} by a_{RS}, we consider 15 samples of initial conditions ($y_0 = [S_0, R_0]$) for each cell within the bounds of the fits generated. These initial condition sets which remained consistent across most simulations were Latin Hypercube sampled from the posterior draws of experimental initial cell population densities (confluences) for Figures 6 and 7. Figures 8 and 9 are the exceptions because we sampled randomly from a uniform distribution. For these plots specifically, we generated 100 randomly sampled real numbers between 0 and 40 for initial conditions, and we sample 100 growth rates and carrying capacity values with consistent rows from the posterior draws with random number generator seed set to 42. As described in Section 2.1, the experimental data consisted of four data categories of 2-hour, 3-hour data series for 20 and

30% initial cell densities. To make all heatmap-like figures, we use parameter averages informed by parameter distributions from the 2-hour and 20% data for each cell type carrying capacities and growth rates (see Appendix B for details regarding inference). While the experimental initial densities ranged from $20-30\%$, inferred y_0 posterior draws ranged from $S_0 \approx 2.4010-45.2049\%$ and $R_0 \approx 0.0049-31.2802\%$, and the random draws from a uniform distribution were within $0-40\%$ for both cells. These initial conditions are representative of different clinical post-surgery tumor burden, allowing for exploration of different residual tumor growth and treatment response following surgical cytoreduction.

We use the numerical approach that follows from [35] to analyze the model. We run all numerical simulations in parallel using NOCONA 0.15.4, MATLAB R2024a_test, and MATLAB R2024b. For the model, we solve the continuous part 1 with MATLAB's ODE solver `ode45`, relative tolerance $\texttt{RelTol} = 1 \times 10^{-4}$, and absolute tolerance $\texttt{AbsTol} = 1 \times 10^{-7}$. For one competition effect parameter pair (a_{SR}, a_{RS}), we report asymptotic behavior of cells by solving model for 500 discrete time steps quantifying long-term treatment, after which we extract the first nine discrete time solutions to explore behavior over a 9-cycle treatment course. For the asymptotic behavior, we consider the uniqueness of the final 100 discrete solutions to capture long-term treatment dynamics while we consider all solutions in the 9-cycle treatment course. The distinct cell abundance values from these selected solutions are then reported using the `uniqetol` built-in MATLAB function and a 1×10^{-3} tolerance. We define cases as thus: if maximum unique value is less than unique tolerance, result is extinction; if the total number of unique values is one, result is a fixed point; if the total number of unique values is more than one, the result is a cycle between more than one value. This cyclic behavior implies that the cell population alternate settling between two or more values over time. Though we save results for up to 16 unique values, we focus on explaining extinction (all solutions $<$ tolerance) and fixed-point persistence (1 unique value) cases in this work. We repeat the numerical exploration steps above for 15 Latin Hypercube Sampled initial conditions y_0 and 40,000 combinations of a_{SR}, a_{RS} defined in Table 3. We report results in MATLAB's `imagesc` maps (Figures 6 and 7) where we use a binary encoding technique to generate unique codes for the possibilities of both cell populations going to mutual extinction, mutual persistence or exclusion from either behavior, for each (a_{SR}, a_{RS}) pair and all initial conditions $y0s$.

3 Results

3.1 Statistical machine learning suggests hybrid model parameters

In this section, we report the results in using model-driven statistical machine learning (Section 2.2) to infer some of the parameters of (1)-(2) from in vitro CP20 and SKOV3 well cultures with and without treatment. Section 3.1.1 discusses a simplified version of

(1) for non-interacting populations, Section 3.1.2 presents the results for the resistant CP20 cells, Section 3.1.3 presents results for the susceptible SKOV3 cell line and Section 3.1.4 draws on the results of Sections 3.1.2-3.1.3 to determine the parameters used in (1)-(2) to demonstrate the effects of the hybrid structure on model stability; these parameters appear in Table 3 as 'Inferred'.

3.1.1 The logistic model for non-interacting populations

In the absence of inter-specific competition, the continuous portion of the hybrid pulsed chemotherapeutic model (Section 2.3) reduces to two uncoupled logistic equations. Specifically, choosing $a_{SR} = 0 = a_{RS}$ in (1) yields two non-communicating initial value problems, each having the general form of

$$\frac{dP}{dt} = \lambda P\left(1 - \frac{P}{K}\right), \quad P(0) = P_0, \tag{3}$$

where λ is a growth rate parameter and K is a saturation, or population carrying capacity, parameter; P_0 represents the initial population size. Assuming that $0 < P_0 < K$, the solution to (3) can be written as

$$P(t) = \frac{K}{1 + \left(\frac{K}{P_0 - 1}\right) e^{-\lambda t}}. \tag{4}$$

According to (1), in the absence of drug intervention, the time dynamics of both S and R follow (4). We used a hierarchical Bayesian inference approach (Section 2.3, Appendix B), implemented using PyMC, to infer the posterior distributions of the parameters corresponding to the sensitive SKOV3 (K_S, λ_S, P_{0_S}) and resistant CP20 (K_R, λ_R, P_{0_R}) cell confluence dynamics.

3.1.2 Resistant (CP20) cell line growth model parameters

In the absence of interactions, (1) reduces to two systems, each of the form of (3). We focus here on (3) for CP20, having growth parameter λ_R, saturation K_R and initial value P_{0_R}. Hierarchical inference on 22 well culture cell population time series data (Table 1) produced 20,000 posterior samples (Section 2.2) for each of the mean value and standard deviation hyperparameter distributions (Table 2) corresponding to each of the model parameter λ_R, K_R and P_{0_R} of (3). Kernel density estimates corresponding to the control and treatment time series data are shown in Figure 2. Control versus treatment hyperparameter posterior distribution means ($\bar{\mu}$) were tested by a two-sided t-test and by the Mann-Whitney U test; hyperparameter standard deviations ($\bar{\sigma}$) were tested by both the Bartlett and Levene tests. Differences in both $\bar{\mu}$ and $\bar{\lambda}$ were significant ($p < 0.001$) for each hyperparameter posterior corresponding to λ_R and K_R (left two columns in Figure 2, c.f. Table 4). The

Table 4: Changes to the hyperparameters governing the growth dynamics of CP20 due to carboplatin treatment at 14μM. The sample mean ($\bar{\mu}$) and sample standard deviation ($\bar{\sigma}$) are reported for each case. Differences in $\bar{\mu}$ and $\bar{\sigma}$, for control versus treated, were significant for each hyperparameter corresponding to both λ_R and K_R.

Parameter	Type	Hyperparameter	$\bar{\mu}$	$\bar{\sigma}$
λ_R (day^{-1})	Control	Mean	1.0916	1.1884×10^{-3}
	Treated	Mean	1.0865	2.1537×10^{-3}
	Control	Standard Deviation	8.4997×10^{-2}	1.0657×10^{-3}
	Treated	Standard Deviation	1.6226×10^{-1}	1.9090×10^{-3}
K_R (% area)	Control	Mean	94.8438	1.5032×10^{-2}
	Treated	Mean	99.8328	1.6237×10^{-2}
	Control	Standard Deviation	2.1571×10^{-1}	2.1739×10^{-1}
	Treated	Standard Deviation	2.4459×10^{-1}	2.5354×10^{-1}

Table 5: Changes to the growth dynamics of CP20 due to carboplatin treatment at 14μM. Sample mean: ($\bar{\mu}$), sample standard deviation ($\bar{\sigma}$), NS: not significant ($p > 0.05$).

Parameter	Type	$\bar{\mu}$	p-value	$\bar{\sigma}$	p-value
λ_R (day^{-1})	Control	1.0924	NS	3.8351×10^{-3}	$p < 0.01$
	Treated	1.0888		7.3419×10^{-3}	
K_R (% area)	Control	99.7245	$p < 0.01$	2.8289×10^{-1}	$p < 0.01$
	Treated	99.6896		3.4012×10^{-1}	

most pronounced relative difference was an increase of 90.9% in the mean of the standard deviation for λ_R.

Next, we approximated the parameter distributions, for each of the parameters λ_R, K_R and P_{0_R}, by drawing 5,000 samples from the hyperparameter distributions for that parameter; for each pair of these sampled hyperparameters, we drew one instance of that parameter from the corresponding parameter distribution (Table 2). The kernel density plot for each parameter is shown in Figure 3. As λ_R and K_R govern the dynamics of (3), we used the tests discussed above to investigated whether carboplatin treatment at 14μM produced differences in $\bar{\mu}$ or $\bar{\sigma}$. The results are reported in Table 5. Most notably, treatment did not alter the sample mean of λ_R, though it did lead to a significant 91.4% relative increase in the standard deviation. The alteration in the mean of K_R was significant but the relative change was small, at an approximate -0.035% adjustment.

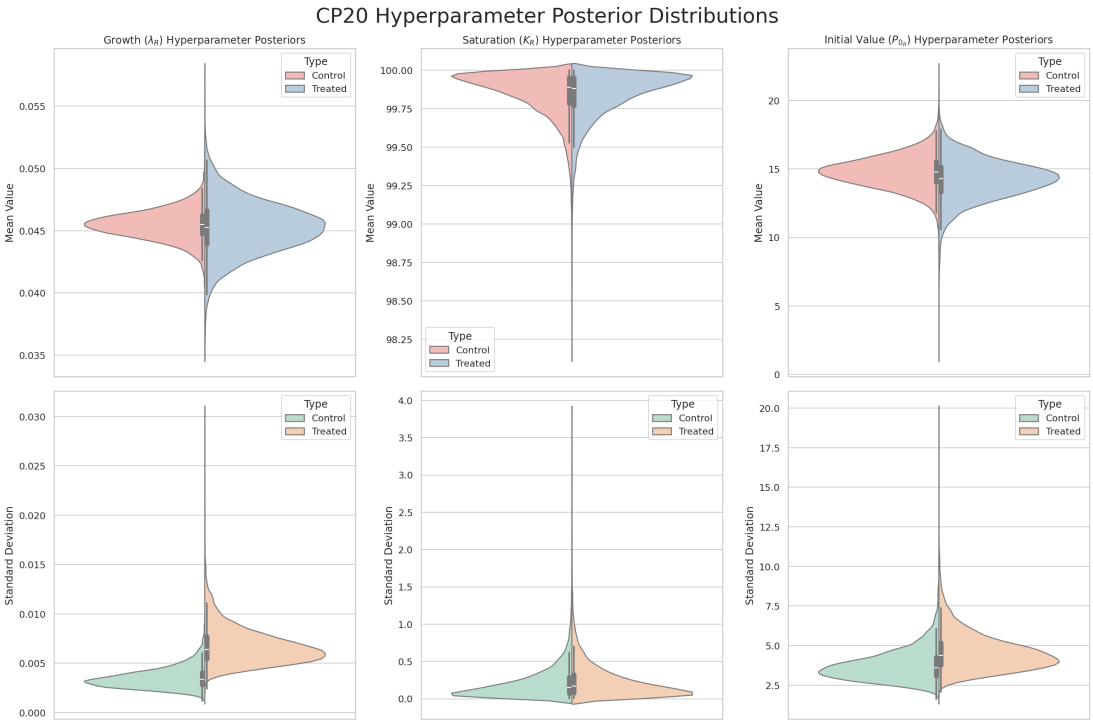

Figure 2: Hyperparameter distributions for the resistant (CP20) cell line growth model parameters without interaction ($a_{SR} = a_{RS} = 0$ in (1)). Growth (left column), Saturation (middle column) and initial value (right column) parameters, compare (1) and (3), are shown for both the control (left violin plot) and treated (right violin plot) cases. Top row: Posterior distributions of the mean value hyperparameter; Bottom row: Posterior distributions of the standard deviation hyperparameter.

3.1.3 Susceptible (SKOV3) cell line growth model parameters

Once more, the non-interacting form of (1) produces (3) with growth parameter λ_S, saturation K_S and initial value P_{0_S} for the susceptible cell line population. Hierarchical inference on 19 well culture cell population time series data (Table 1) produced 20,000 posterior samples (Section 2.2) for each of the mean value and standard deviation hyperparameter distributions (Table 2) corresponding to each of the model parameter λ_S, K_S and P_{0_S} of (3). Kernel density estimates corresponding to the control and treatment time series data are shown in Figure 4. As in Section 3.1.2, control versus treatment hyperparameter posterior distribution means were tested by a t-test and a Mann-Whitney U test while standard deviations were tested with the Bartlett and Levene tests (c.f. Table 6). In comparing the control versus treatment hyperparameter posteriors corresponding to growth (λ_S): $\bar{\mu}$ was significantly different for both the mean value and standard deviation posteriors ($p < 0.05$,

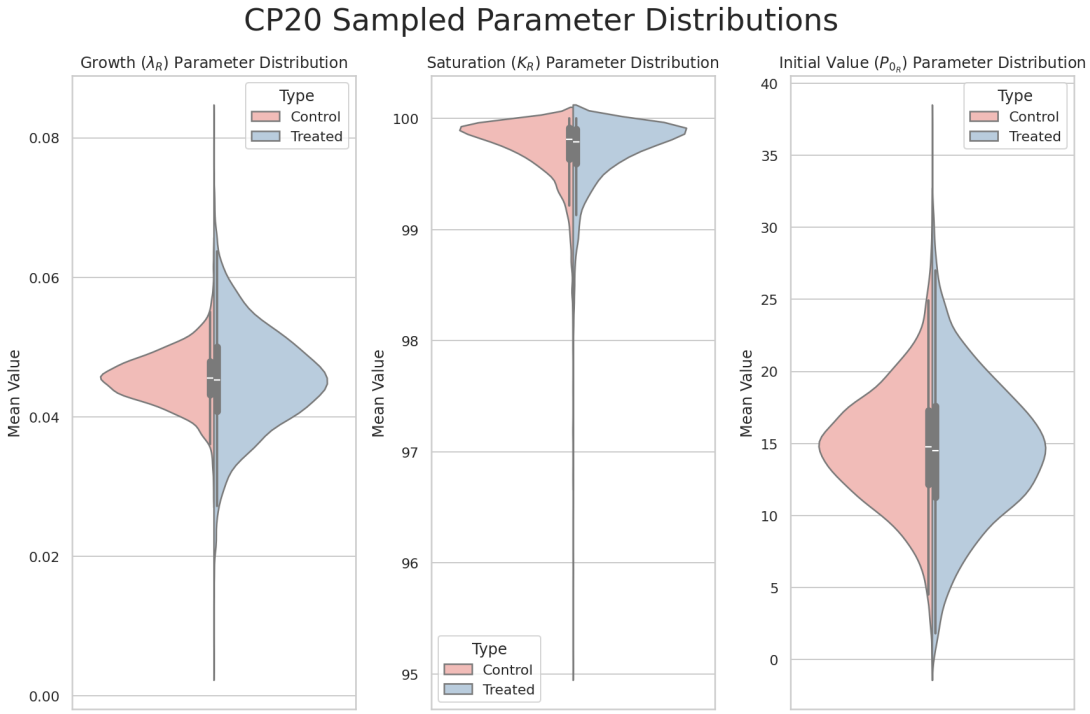

Figure 3: Sampled parameter distributions for the resistant (CP20) cell line growth model parameters without interaction ($a_{SR} = a_{RS} = 0$ in (1)). Growth (left column), Saturation (middle column) and initial value (right column) parameters.

all tests). However, $\bar{\sigma}$ was not significantly different for the mean value posterior whereas it was ($p < 0.05$, both tests) for the standard deviation posterior. For hyperparameter posteriors corresponding to saturation (K_S): differences in $\bar{\mu}$ were significant only for the standard deviation hyperparameter, while $\bar{\sigma}$ was statistically different ($p < 0.05$, all tests) for both hyperparameter distributions.

As in Section 3.1.2, we approximated the parameter distributions of λ_S, K_S and P_{0_S} by drawing 5,000 samples from the hyperparameter distributions and using those samples to draw from the corresponding parameter distribution (Table 2). The kernel density plot for each parameter is shown in Figure 3. As λ_S and K_S govern the dynamics of (3), we used the tests discussed above to investigated whether carboplatin treatment at 14μM produced differences in $\bar{\mu}$ or $\bar{\sigma}$. The results are reported in Table 7. In contrast to CP20, the mean value of the growth parameter (λ_S) for SKOV3 cells was altered by 14μM carboplatin treatment; the relative change in $\bar{\mu}$ was 8.9294%. Similar to CP20, there was also a shift in $\bar{\mu}$ for K_S but, again, the relative shift was small at 0.0139%.

Table 6: Changes to the hyperparameters governing the growth dynamics of SKOV3 due to carboplatin treatment at 14μM. The sample mean ($\bar{\mu}$) and sample standard deviation ($\bar{\sigma}$) are reported for each case. Differences in $\bar{\mu}$ and $\bar{\sigma}$, for control versus treated, were significant for each hyperparameter corresponding to both λ_R and K_R.

Parameter	Type	Hyperparameter	$\bar{\mu}$	$\bar{\sigma}$
λ_S (day^{-1})	Control	Mean	1.0794	2.2355×10^{-3}
	Treated	Mean	1.1807	2.2750×10^{-3}
	Control	Standard Deviation	6.6179×10^{-3}	2.0909×10^{-3}
	Treated	Standard Deviation	6.2950×10^{-3}	2.1270×10^{-3}
K_S (% area)	Control	Mean	99.8717	1.2256×10^{-1}
	Treated	Mean	99.8739	1.1997×10^{-1}
	Control	Standard Deviation	1.7799×10^{-1}	1.8150×10^{-1}
	Treated	Standard Deviation	1.6484×10^{-1}	1.6611×10^{-1}

Table 7: Changes to the growth dynamics of SKOV3 due to carboplatin treatment at 14μM. Sample mean: ($\bar{\mu}$), sample standard deviation ($\bar{\sigma}$), NS: not significant ($p > 0.05$).

Parameter	Type	$\bar{\mu}$	p-value	$\bar{\sigma}$	p-value
λ_S (day^{-1})	Control	1.0807	$p < 0.01$	7.2007×10^{-3}	$p < 0.01$
	Treated	1.1772		6.9254×10^{-3}	
K_S (% area)	Control	99.7741	$p < 0.01$	2.4312×10^{-1}	$p < 0.05$
	Treated	99.7880		2.2091×10^{-1}	

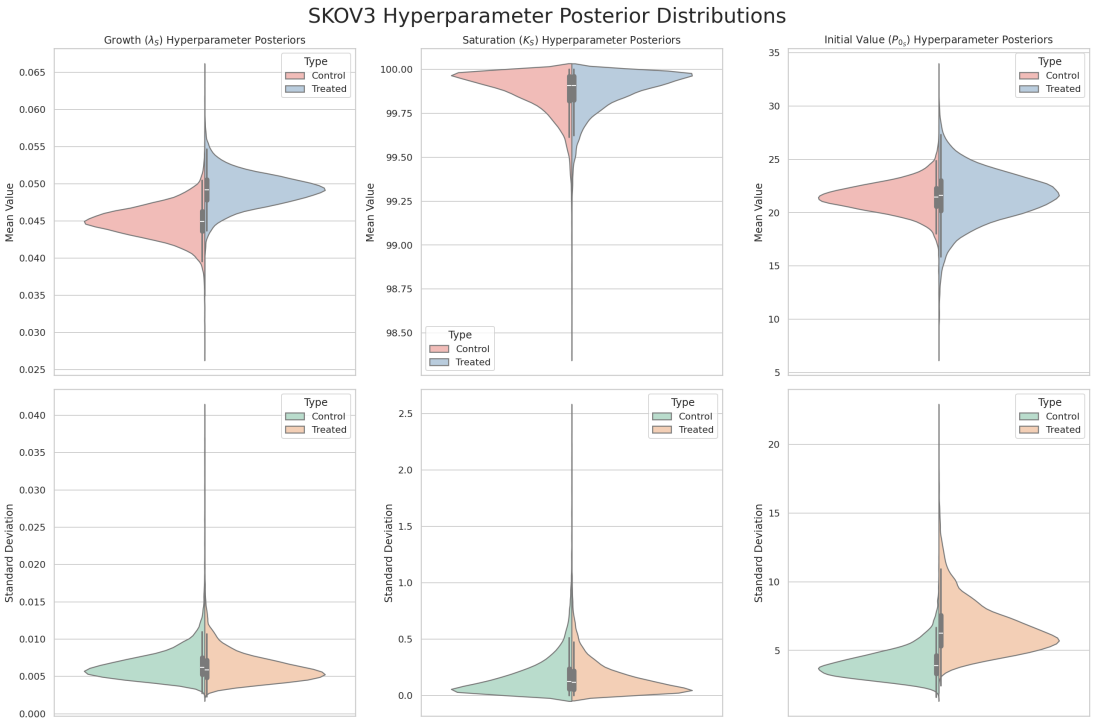

Figure 4: Hyperparameter distributions for the susceptible (SKOV3) cell line growth model parameters without interaction ($a_{SR} = a_{RS} = 0$ in (1)). Growth (left column), Saturation (middle column) and initial value (right column) parameters, compare (1) and (3), are shown for both the control (left violin plot) and treated (right violin plot) cases. Top row: Posterior distributions of the mean value hyperparameter; Bottom row: Posterior distributions of the standard deviation hyperparameter.

3.1.4 Parameter selection for a simple pulsed hybrid model

In this section, Bayesian inference-based statistical machine learning (Section 2.2 and Appendix B) was used to infer growth, saturation and initial condition parameter distributions from in vitro experiments. As (1)-(5b) is deterministic, we use mean values from the posterior distributions as point estimates for λ_R, and K_R (Table 5) along with λ_S and K_S (Table 7). Since a statistically significant differences was not found between the mean values of the control and treatment cases for λ_R (Table 5), we take λ_R to be equal to the control case mean value ($\lambda_R = 1.0924$) and select $Q = 0$ in (5b). Since a statistically significant difference between the mean values of the control and treatment cases was found for λ_S (Table 7), we select the initial value for λ_S to coincide with that of the control case ($\lambda_S = 1.0807$) and choose P to coincide with the relative difference ($P = 0.0893$) between the inferred values of λ_S of the treatment versus control cases.

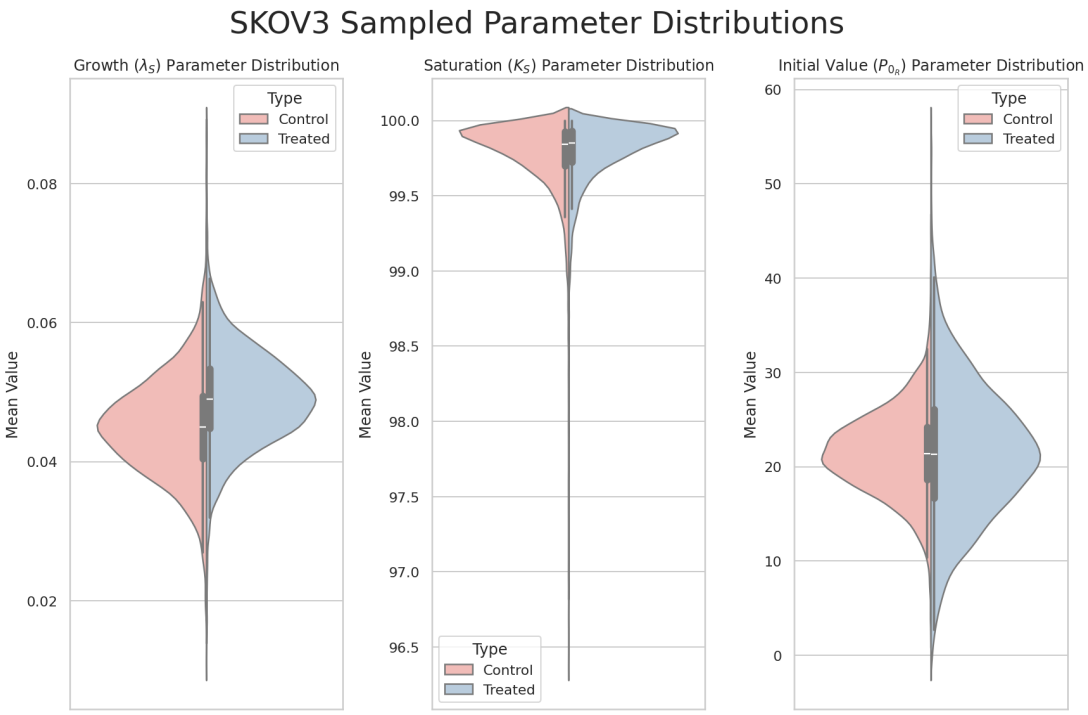

Figure 5: Sampled parameter distributions for the susceptible (SKOV3) cell line growth model parameters without interaction ($a_{SR} = a_{RS} = 0$ in (1)). Growth (left column), Saturation (middle column) and initial value (right column) parameters.

Significant differences were found between the mean values of control versus treatment for both of the saturation parameters K_R and K_S (Table 5 and Table 7). Namely, K_R decreased slightly while K_S increased slightly. However, the relative change was so small that $N = 29$ treatments would be needed to decrease K_R by 1% of its initial value while $N = 17$ treatments would be needed to raise K_S by 0.226% to its theoretical maximum of 100. Since our reference clinical trials used a maximum of nine treatments [36], we neglect the small changes in the saturation parameters and choose K_R and K_S to coincide with the mean values inferred from the control case growth data ($K_R = 99.7245$ and $K_S = 99.7741$, respectively). The inferred values used in the model are reported in Table 3.

3.2 Existence of positive equilibrium

Identifying positive equilibrium is a central tenet in understanding long-term behavior of interacting populations; in the hybrid pulsed chemotherapeutic model presented in Section 2.3, these populations are precisely sensitive and resistant cancer cells. To establish conditions on the existence of positive equilibrium, we considered two cases. The first of

which is when the inter-specific competition effect of R on S and of S on R multiply to 1, in other words, when $a_{SR}a_{RS} = 1$. However, before we examine this case, we provide a necessary condition for the existence of a positive equilibrium of the aforementioned model. See Appendix A for the proofs of the results contained in this subsection.

Theorem 1. *If the hybrid pulsed chemotherapeutic model contains a positive equilibrium, then*

$$\lambda_S T - \ln\left(\frac{1}{1-p}\right) > 0 \text{ and } \lambda_R T - \ln\left(\frac{1}{1-q}\right) > 0.$$

Returning to the case where $a_{SR}a_{RS} = 1$, the resulting system of equations (see Appendix A equation (7)) exhibit linear dependence; using this, we establish an additional necessary condition for the existence of positive equilibrium.

Theorem 2. *Suppose $a_{SR}a_{RS} = 1$, then the hybrid pulsed chemotherapeutic model has no positive equilibrium if*

$$\frac{K_R\lambda_S a_{SR}}{\lambda_R K_S}\left(\lambda_R T - \ln\left(\frac{1}{1-q}\right)\right) \neq \lambda_S T - \ln\left(\frac{1}{1-p}\right)$$

or equivalently

$$\lambda_R T - \ln\left(\frac{1}{1-q}\right) \neq \frac{\lambda_R K_S a_{RS}}{K_R\lambda_S}\left(\lambda_S T - \ln\left(\frac{1}{1-p}\right)\right).$$

In the case where $a_{SR}a_{RS} \neq 1$, we are able to establish a stronger result; a condition that is not only necessary but also sufficient.

Theorem 3. *Let $a_{SR}a_{RS} \neq 1$. The hybrid pulsed chemotherapeutic model contains a positive equilibrium if and only if*

$$\frac{a_{RS}a_{SR}\lambda_S}{K_S}\left(\lambda_R T - \ln\left(\frac{1}{1-q}\right)\right) > \frac{a_{RS}\lambda_R}{K_R}\left(\lambda_S T - \ln\left(\frac{1}{1-p}\right)\right) > \frac{\lambda_S}{K_S}\left(\lambda_R T - \ln\left(\frac{1}{1-q}\right)\right)$$

for $a_{RS}a_{SR} > 1$, or

$$\frac{a_{RS}a_{SR}\lambda_S}{K_S}\left(\lambda_R T - \ln\left(\frac{1}{1-q}\right)\right) < \frac{a_{RS}\lambda_R}{K_R}\left(\lambda_S T - \ln\left(\frac{1}{1-p}\right)\right) < \frac{\lambda_S}{K_S}\left(\lambda_R T - \ln\left(\frac{1}{1-q}\right)\right)$$

for $a_{RS}a_{SR} < 1$.

By substituting all except the inter-specific competition effect parameters with values from Table 3, the inequalities in Theorem 3 are reduced to

$$a_{RS}a_{SR} > 0.9372\,a_{RS} \;\&\; 0.9372\,a_{RS} > 1$$

for $a_{RS}a_{SR} > 1$, or

$$a_{RS}a_{SR} < 0.9372\,a_{RS} \;\&\; 0.9372\,a_{RS} < 1$$

for $a_{RS}a_{SR} < 1$.

Therefore, from the results above, we have established a necessary condition for the existence of positive equilibrium regardless of the value of $a_{SR}a_{RS}$. Moreover, in the case where the product $a_{SR}a_{RS}$ equals 1, we established another necessary condition. Furthermore, in the case where $a_{SR}a_{RS} \neq 1$ we were able to establish not only a necessary condition but also sufficient; this provides a characterization for the existence of positive equilibrium in the case where the product $a_{SR}a_{RS}$ is not equal to 1.

3.3 Hybrid model computational analysis

The presence of different cell types in a system requires some limiting effect on one cell due to the presence of the other. We quantify these effects as inter-specific competition rates of the resistant cells R on the sensitive cells S (a_{SR}) and S on R (a_{RS}). Parameter sweeps of (a_{SR}, a_{RS}) combinations adding up to 40,000 are explored to assess the behavior of each cell type in community. The figures below are based on these parameter explorations with 15 sampled initial conditions, and average posterior growth rates and carrying capacities. Specifically, figures 6 and 7 show characterizations of extinction, persistence (positive non-zero fixed point), and exclusion possibilities for at least one initial condition y_0. With exclusion specifically, we report the possibility of a population heading to a behavior and the other population not heading to the same. For example, to report R-exclusion from extinction, we check where S goes extinct and R does not for at least one out of 15 y_0s, implying that R goes to a fixed point or exhibits a cyclic behavior in which it is still changing over the entire treatment course.

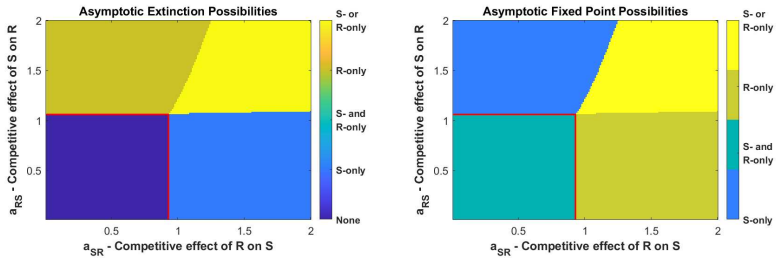

(a) (b)

Figure 6: Bifurcation map of long-term possibilities of extinction (7a) and persistence (7b) of tumor cells in an inter-specific competition space where 15 initial conditions are considered. Red boundary on both figures represent the region where Theorem 3 is satisfied. "None" represents points where behavior is absent. "S-only" represents points where only the sensitive cells (S) show possibilities. "R-only" points where only the resistant cells (R) show possibilities. "S- and R- only" represents points where both S and R show possibilities. "S- or R- only" represents points where either S or R show possibilities.

The bifurcation heatmaps in Figure 6 represent asymptotic cell population dynamics under competition. That is, the maps show the possibility of extinction (Figure 6a) and persistence (Figure 6b) of S and R, for 500 treatment cycles ($\sim$ 30 years of 21-day interval treatments) as a_{SR} increases from left to right and a_{RS} increases from bottom to top. The rates increase from 0.01 to 2 at a 0.01 step size. This map particularly reports terminal behavior by considering the population dynamics in the terminal 100 treatment administrations. In Figure 6a, the purple "None" region where $a_{SR} \in [0.01, 0.93]$ and $a_{RS} \in [0.01, 1.06]$ indicates the parameter space where none of the cell populations show possibilities of extinction together or individually. This parameter space colored teal "S- and R-only" in Figure 6b presents possibilities of coexistence fixed points for both S and R. The red line bounding this region represents the parameter space that satisfies the condition from Theorem 3 which is necessary and sufficient for the existence of a positive equilibrium. Next is the blue "S-only" region in Figure 6a that represents the competition parameters $a_{SR} \in [0.94, 2]$ and some $a_{RS} \in [0.01, 1.09]$ where only S goes extinct for at least one y_0. The corresponding region in Figure 6b shows that only R reaches a positive fixed point in this parameter space, a behavior we define as S-exclusion, seeing as R excludes S from heading to a non-zero fixed point in the system. We see that the region where R goes extinct alone (light yellow "R-only" region) in Figure 6a is where S excludes R in Figure 6b (blue "S-only" region). This happens for some $a_{SR} \in [0.01, 1.25]$ and all $a_{RS} \in [1.07, 2]$ in Figure 6b. The yellow regions in both maps represents points where either S excludes R or vice versa from extinction (Figure 6a) or persistence (Figure 6b), highlighting a mutually exclusive bistable dynamics between both populations driven by different initial conditions. Figure 6a reports a zero possibility of both cells going extinct together.

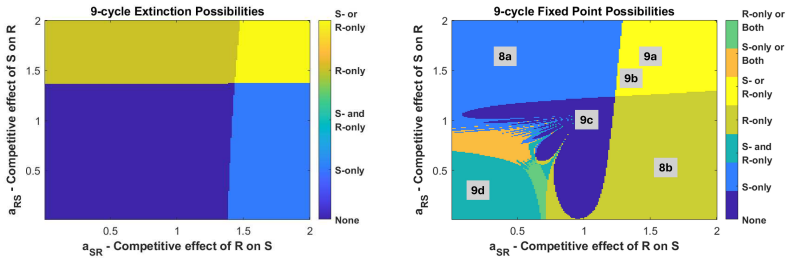

(a) (b)

Figure 7: Bifurcation map of 9-treatment-cycle possibilities of extinction (7a) and persistence (7b) of tumor cells in an inter-specific competition space where 15 initial conditions are considered. "None" represents points where behavior is absent. "S-only" represents points where only the sensitive cells (S) show possibilities. "R-only" points where only the resistant cells (R) show possibilities. "S- and R- only" represents points where both S and R show possibilities. "S- or R- only" represents points where either S or R show possibilities. "S-only or Both" represents points where either S or both S and R show possibilities. "S- or R- only" represents points where either R or both S and R show possibilities.

Here, we see the possibility of extinction (Figure 7a) and persistence (Figure 7b) of S and R, for 9 treatment cycles ($\sim 5-6$ months of treatment). Though Figure 7a map has a 4-quadrant behavior like the long-term extinction possibilities in 6, the purple region which classifies non-extinction possibilities in this 9-treatment-cycle map is larger with more parameters that result in a positive solution: $a_{SR} \in [0.01, 1.38]$ and $a_{RS} \in [0.01, 1.37]$. Not all these positive solutions are however positive fixed points as in Figure 7b). That is, this positive solution region diversifies into mutual fixed point possibilities and exclusion from fixed point possibilities. Both cell populations only coexist stably for some $a_{SR} \in [0.01, 0.9)$ and some $a_{RS} \in [0.01, 1.04)$. Some of these fixed point regions also report partial R-exclusion (orange region labeled "S-only or Both") or partial S-exclusion (green region labeled "R-only or Both"). These exclusion behaviors particular appear near the actual majority exclusion region. That is, "S-only or Both" appears closer to the top blue "S-only" space, while "R-only or Both" occurs near the teal "R-only" space. The butterfly-like purple "None" region represents parameter combinations where the population solutions are still cycling between more than one positive value over the treatment course instead of a fixed point. This part of the parameter space eventually settles into coexistence or exclusion of the populations long-term as in Figure 6b. In both figures, the yellow mutually exclusive "S- or R-only" parameter spaces are notably unequal in size. This is because for some $a_{SR} \in (1.3, 1.47)$ and some $a_{RS} \in (1.2, 1.38)$ which fall in the "None" region in Figure 7a, S and R also go to a fixed point or more non-zero positive solutions for some initial conditions. Therefore Figure 7b reports a mutually exclusive dynamics of one or more

positive solutions for these competition values.

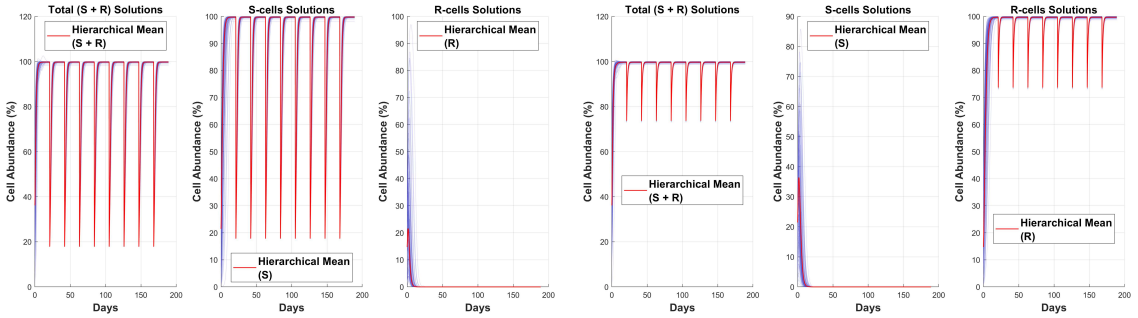

(a) $a_{SR} = 0.5, a_{RS} = 1.6$ (b) $a_{SR} = 1.5, a_{RS} = 0.6$

Figure 8: Trajectory plots of tumor cells' abundance over time with 100 posterior samples of parameters (blue) vs their mean (red) for parameter sets $(a_{SR}, a_{RS}) = (8a) : (0.5, 1.6), (8b) : (1.5, 0.6)$. For each figure, left panel represents the sum of the individual solutions in the middle and right panels, middle panel represents solutions for S population and the right panel represents the solutions for the R population.

Figure 8 shows the solution trajectories of different parameters sets sampled from the posterior against the mean of the draws. These parameter pairs were selected from the exclusion regions labeled 8a and 8b in Figure 7b to show how the solutions of 100 sampled initial conditions between 0 and 40 and growth-capacity combinations align with the behavior reported in Figure 7. Each figure recovers the expected behavior from the fixed point map. That is, Figure 8a which displays solutions with low competition effect of R on S ($a_{SR} = 0.5$) and high competition effect of S on R ($a_{RS} = 1.6$) shows R-exclusion. Contrarily, Figure 8b which displays solutions with high competition effect of R on S ($a_{SR} = 1.5$) and low competition effect of S on R ($a_{RS} = 0.6$) shows S-exclusion.

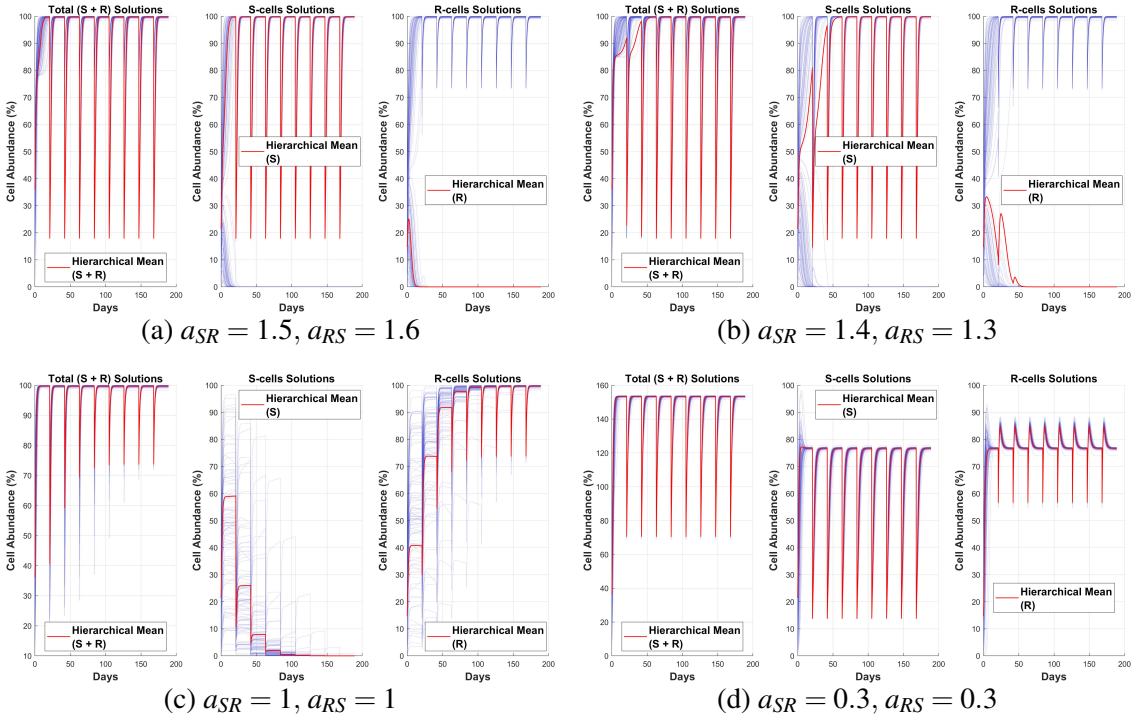

(a) $a_{SR} = 1.5, a_{RS} = 1.6$ (b) $a_{SR} = 1.4, a_{RS} = 1.3$

(c) $a_{SR} = 1, a_{RS} = 1$ (d) $a_{SR} = 0.3, a_{RS} = 0.3$

Figure 9: Trajectory plots of tumor cells' abundance over time with 100 posterior samples of parameters (blue) vs their mean (red) for parameter sets $(a_{SR}, a_{RS}) = (9a) : (1.5, 1.6), (9b) : (1.4, 1.3), (9c) : (1, 1), (9d) : (0.3, 0.3)$. For each figure, left panel represents the sum of the individual solutions in the middle and right panels, middle panel represents solutions for S population and the right panel represents the solutions for the R population.

Figure 9 shows the solution trajectories for parameter pairs selected from the regions labeled 9a to 9d in Figure 7b. In Figure 9a, inter-specific competition effects ($a_{SR} = 1.5, a_{RS} = 1.6$) lead to mutual exclusivity of either S-exclusion or R-exclusion, with the mean solution also being R-exclusion. Mid-parameter space exploration seen in Figure 9c ($a_{SR} = a_{RS} = 1$) shows how both cell population solutions keep changing values throughout the treatment course instead of reaching a positive non-zero fixed point, while the mean parameter values lead the overall population to S-exclusion. Figure 9b's parameter pair ($a_{SR} = 1.3, a_{RS} = 1.3$) also display similar behavior as Figure 9c, where some initial conditions leads to cell populations taking more days to settle into fixed points or exclusion as we see with the mean parameters' solution. Low competition effect of R on S ($a_{SR} = 0.5$) and S on R ($a_{RS} = 0.6$) as seen in Figure 9d leads to stable fixed point for all samples. All parameter pairs report totals that are close to 100% with $S + R > 100\%$ when $a_{SR} = 0.5$ and $a_{RS} = 0.6$.

3.4 Effective treatment implications on cell growth

Statistical analysis from section 3.1.3 showed that treatment may alter cell growth significantly. Motivated by this result, we update our model from section 2.3 by considering additional discrete-time dynamics to show how the growth rate of drug-sensitive cells (S) is affected by treatment. For all these cases, we assume this treatment effect on cell growth is independent of treatment concentration. Please refer to Tables 3, 5 and 7 for parameter values.

Case (a): S starts growing at the initial growth rate $\lambda_S(\text{control}) = 1.0807$ and then peaks at rate $\lambda_S(\text{treated}) = 1.1772$ of S for the remaining treatment pulses. Similarly, R starts growing at the initial growth rate $\lambda_R(\text{control}) = 1.0924$ and then heads to the rate $\lambda_R(\text{treated}) = 1.0888$ of R for the remaining treatment pulses. (See Equation 5a and Figure 10a).

Case (b): The change in growth dynamics for this case is described in section 3.1.4. That is, S starts growing at the initial rate $\lambda_S(\text{control}) = 1.0807$ and increases at a constant rate $P = 0.0893$ at each treatment pulse, where P is the statistically significant percentage difference between the growth dynamics of control vs treated data. R, however, grows at the constant rate $\lambda_R(\text{control}) = 1.0924$ due to the changes in growth dynamics of control vs treated data being statistically insignificant. (See Equation 5b and Figure 10b).

Case (c): The resistant cell lines used in the experiment attained resistance by continuous exposure to treatment. This motivated the assumption that the growth of S tends to R in theory. Therefore, to obtain a smooth approximation of the treatment effect on λ_S (see Equation 5c and Figure 10c), we fit a quadratic polynomial $\text{pol}(x) = \text{polC}_0 + \text{polC}_1 x + \text{polC}_2 x^2$ to the observed growth parameters, where polC is the coefficient of the polynomial.

The discrete-time equations for the three cases are written as:

$$\begin{aligned} \lambda_{S_{T+1}} &= 1.0807 \text{ for } t = 1 \text{ and } \lambda_{S_{T+1}} = 1.1772 \text{ for } t = 2, \cdots, 9 \\ \lambda_{R_{T+1}} &= 1.0924 \text{ for } t = 1 \text{ and } \lambda_{S_{T+1}} = 1.0888 \text{ for } t = 2, \cdots, 9 \end{aligned} \tag{5a}$$

$$\begin{aligned} \lambda_{S_{T+1}} &= 1.0893 \cdot \lambda_S(T^-) \\ \lambda_{R_{T+1}} &= 1.0924 \end{aligned} \tag{5b}$$

$$\begin{aligned} \lambda_{S_{T+1}} &= \text{polC}_0 + \text{polC}_1 \cdot i + \text{polC}_2 \cdot i^2, \quad i = 1, \cdots, 9 \\ \lambda_{R_{T+1}} &= 1.0924 \text{ for } t = 1 \text{ and } \lambda_{S_{T+1}} = 1.0888 \text{ for } t = 2, \cdots, 9 \end{aligned} \tag{5c}$$

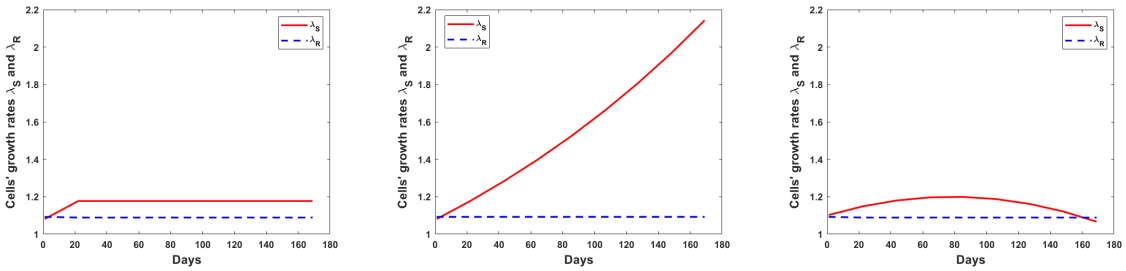

(a) (b) (c)

Figure 10: The growth rate λ_S of the sensitive cells S is represented with solid red lines, and the growth rate λ_R of the resistant cells R is represented with dashed blue lines. Panel (a) corresponds to case (a) described above: $[\lambda_S, \lambda_R] = [1.0807, 1.0924]$ for the first treatment cycle $t = 1$ before treatment starts on day 21, and they reach maximum values $[1.1772, 1.0888]$ for $t = 2, \cdots, 9$ (days 22 - 189). Panel (b) corresponds to case (b): $[\lambda_S, \lambda_R] = [1.0807, 1.0924]$ when $t = 1$, and λ_S increases by 8.93% at each $t = 2, \cdots, 9$ (days 22 - 188) while λ_R has no significant change. Panel (c) corresponds to case (c): $[\lambda_S, \lambda_R] = [1.0807, 1.0924]$ when $t = 1$. When $t = 2, \cdots, 9$, λ_S approaches $\lambda_R = 1.0888$ smoothly, with the stepwise behavior approximated using a quadratic polynomial.

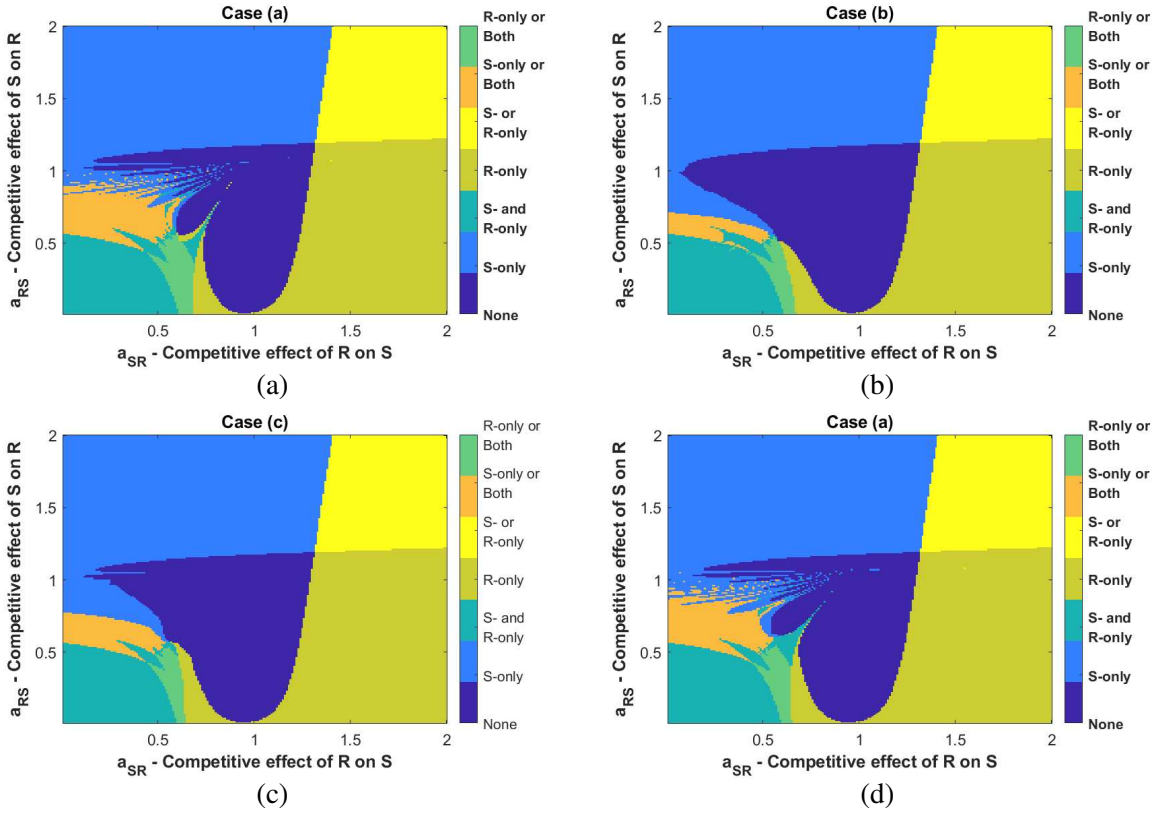

Figure 11: Bifurcation map of 9-treatment-cycle possibilities of tumor cells in an interspecific competition space that incorporates growth changes between treatment administrations with 15 initial conditions considered. "None" represents points where behavior is absent. "S-only" represents points where only sensitive cells (S) shows possibilities. "R-only" represents points where only resistant cells (R) shows possibilities. "S- and R- only" represents points where both S and R show possibilities. "S- or R- only" represents points where either S or R show possibilities. "S-only or Both" represents points where either S or both S and R show possibilities. "S- or R- only" represents points where either R or both S and R show possibilities. Panel (a): After first treatment cycle, both cells' growth rates peak at their respective post-treatment growth rates. Panel (b): Growth rate λ_S of S changes at the percentage $P = 0.0893$ after each treatment pulse. Panel (c): Growth rate λ_S changes at each treatment pulse based on a quadratic polynomial model approximation. Panel (d): Reference result from Figure 7b which uses constant growth rates given in Table 3.

Figures 11a, 11b and 11c correspond to cases (a), (b) and (c) respectively from above. The three cases of growth alteration head to the same behavior long-term as in Figure 6b. However, case (b) appears to head faster to the asymptotic behavior unlike the other cases, while case (a) appears the slowest. The behavior observed in case (a) model also signif-

icantly mirrors that in base model as in Figure 11d. Comparing coexistence regions, the three cases show significant differences in the behavior with case (a) allowing for more competition coefficients where both cells coexist in addition to competitive exclusion and case (b) reports the least possibilities. That is, all cases of growth alterations show similar possibilities of only coexistence, but the growth alteration in case (a) leaves room for more coexistence opportunities while case (b) reports more competitive exclusion possibilities.

4 Discussion

A key path to exploring mixed-time interactions accurately is by accounting for the hybrid dynamics within these systems. This includes representing hybrid processes as is. Applications which are often a combination of continuous dynamics and periodic interventions, like ecological management, agricultural pest control, resource harvesting, or disease treatment, can be fully analyzed with all components intact. In this work, we presented a computational stability analysis framework for hybrid models of continuous and discrete processes, in combination with statistical parameter inference and numerical bifurcation analysis. We combined this methodological study with an illustrative application to cancer treatment and show how our approach can efficiently characterize system behaviors across parameter spaces, without analytical derivations that are often infeasible. To account for the instability that arises from discrete events being sensitive to the starting points of systems, we also incorporated multiple initial states of our focus system for more robust characterization of behaviors.

In our illustrative example with competing cancer cells, the asymptotic map (500 treatment cycles) depicts the system's long-term behavior if a patient received 500 periodic treatments on a continuous course. Although this is clinically impossible, the results provide a long-term direction of shorter clinically-relevant cycles like the 9 treatment cycles plan. Observing this long-term outcomes helps establish the principle: if hybrid models can capture a system's mechanisms, computational stability analysis can reveal how variables like growth and competition dynamics determine outcomes. The absence of co-extinction regions across all results would indicate that complete tumor eradication is unlikely under the modeled growth and treatment protocol. The fixed point possibilities region reported by the 500-cycle treatment regimen shows stable coexistence of the cell populations long-term as proven by Theorem 3 which characterizes the existence of a positive solution for the hybrid model. These regions of stable coexistence could be interpreted as cells being able to collectively repair and reproduce rapidly, with neither population driving the other extinct. On the other hand, the 9-cycle treatment regimen reporting fixed point possibilities revealed complex parameter regions for similar competition parameters as the asymptotic result. These points in the shorter treatment protocol result in mostly stable coexistence with competitive exclusion dependent on initial condition, where the latter is

an area of sensitivity for discrete processes. Statistical analysis from Section 3.1.2 and 3.1.3 also show the persistent behavior of the sensitive cells (S) where treatment is known to increase the rate of rebound due to mechanisms like an increased metastasis rate and developing resistance in susceptible cells that survive. This might explain P and Q (Table 3), where Q (CP20) shows no further change while P reflects a flux of effects. Furthermore, we also observe other predictable behaviors in the 9-cycle treatment regimen. The initial conditions in this regimen corresponding to different post-surgical residual disease states showed slower growth trajectories at lower starting densities, as would be expected clinically. However, this 9-cycle model also predicts rebounds to stable states or capacity after treatment cessation, consistent with clinical observations of recurrence. This can be interpreted as treatment failure or relapse depending on the initial tumor state of a patient. Such hypothetical interpretations demonstrate how computational stability analysis, when applied to appropriately validated models, could inform decision-making about the timing, intensity, or combinations of pulse events.

The key limitation remains model fidelity: our framework can efficiently analyze model behavior, but cannot compensate for biological mechanisms not represented in the model structure. This is because our hybrid cancer model is a simplified illustration chosen for its clear mathematical structure and accessible parameterization from available data, to demonstrate how our computational methods can extract insights from hybrid models when analytical results are already intractable. Although we can find the non-trivial existence of positive equilibria for our model as seen in Section 3.2 and Appendix A, we cannot establish clinically sound stability conditions due to model limitations. In real cancer literature, models are considerably more sophisticated in describing tumor dynamics mechanisms far more complex than our two-population competition model. For example, existing models that account for both sensitive and resistant subpopulations have shown how treatment intensity and scheduling [15], growth and functionality of immune cells under changing diets [20], cell facilitation [27], cell-level competition [23, 37] and genetic alterations [31] drive coexistence, exclusion, or dominance of resistant cells. These recent works [23, 37] emphasize that tumor heterogeneity and localized conditions strongly shape resistance pathways, and also buttress the importance of models that can account for multiple interacting scales [31] and immunosuppression [28, 33]. Our four-quartet methodology consisting of hybrid models, Bayesian parameter inference, statistical and computational stability analysis provides a more realistic way of parameterizing and exploring continuous processes and discrete events from experimental data in cancer dynamics, which should be paired with increasingly sophisticated models.

The computational stability analysis framework presented here is not specific to cancer models and can be applied to any hybrid dynamical system where discrete events punctuate continuous dynamics. Potential applications include: seasonal wildlife management with periodic culling or stocking, agricultural systems with scheduled pesticide or fertilizer application, infectious disease control with vaccination campaigns, and fisheries with harvest

seasons. Our method can efficiently map how different drivers of these systems interact to give rise to different outcomes, from transient to long-term. Ongoing studies with this method updates the framework to be adaptive to the size and drivers of different systems, therefore allowing for descriptions of much more complex scenarios. Future methodological extensions could incorporate characteristics such as spatial structures and stochasticity that account for fluctuations in biological and environmental continuous-discrete processes. With the cancer illustration in particular, extensions can scale to integrate immune cells dynamics and combination or sequential therapies to study how these updates can possibly eliminate tumor cell populations. Step-by-step updates could be in the form of studying cell-cell interactions like [23, 37] and adhesion [10] in relation to the movement of cells and cancer takeover. That is, by simulating neighborhood cell-level competition, we can test if the coexistence and exclusion patterns observed in our results appear after relaxing the assumption of well-mixed tumor cells population in this adjuvant setting. Further breakthrough work can extend to inform unique parameters and hybrid models with individual-level data that accounts for the heterogeneity of different tumor populations, so that adjustments to treatment cycles and parameters can be explored to assess treatment responses and outcomes. Overall, this work contributes broadly to establishing computational stability analysis as an accessible and powerful tool for studying hybrid models across applied interdisciplinary domains, circumventing the often-prohibitive analytical challenges these systems present.

Acknowledgment(s)

We would like to thank Dr. Komariah Palle and the Palle Lab from the Department of Cell Biology and Biochemistry, TTUHSC, for generously supplying the cell lines, media, and reagents used in our in-vitro experiments. We also sincerely appreciate Dr. Mayomikun Olawale from Babcock University Teaching Hospital (BUTH), for his invaluable discussions and insights on oncology specifics.

Disclosure statement

The authors report there are no competing interests to declare.

Authors' contribution statement

Boluwatife Awoyemi: Conceptualization; Software - Hybrid Model Simulations; Methodology; Writing – original draft; Writing – review and editing.
Robert Young: In vitro experiments; Methodology; Writing – original draft; Writing –

review and editing.
Bradley Vigil: Formal mathematical analysis; Writing – original draft; writing – review and editing.
Naresh Sah: In vitro experiments; Writing – review and editing.
Travis Thompson: Statistical inference; Methodology; Supervision; Writing – original draft; Writing – review and editing.
Sharilyn Almodovar: In vitro experiments; Supervision; Writing – review and editing.
Amanda Laubmeier: Conceptualization; Methodology; Supervision; Writing – review and editing.

Funding

This work was supported, at least in part, by the NSF LEAPS-MPS Grant 2137694, NSF CAREER Grant 2441043, and the TTUHSC School of Medicine Dean's Office and Office of Research and Innovation.

References

[1] Thomas Bayes and Richard Price. "LII. An Essay towards Solving a Problem in the Doctrine of Chances". In: *The Royal Society, Philosophical Transactions* 53 (1763), pp. 370–418.

[2] Vladimir A Kuznetsov et al. "Nonlinear dynamics of immunogenic tumors: parameter estimation and global bifurcation analysis". In: *Bulletin of mathematical biology* 56.2 (1994), pp. 295–321.

[3] Denise Kirschner and John Carl Panetta. "Modeling immunotherapy of the tumor–immune interaction". In: *Journal of mathematical biology* 37.3 (1998), pp. 235–252.

[4] John Carl Panetta. "A mathematical model of drug resistance: heterogeneous tumors". In: *Mathematical biosciences* 147.1 (1998), pp. 41–61.

[5] Abdelkader Lakmeche and Ovide Arino. "Nonlinear mathematical model of pulsed-therapy of heterogeneous tumors". In: *Nonlinear Analysis: Real World Applications* 2.4 (2001), pp. 455–465.

[6] Lisette G de Pillis, Ami E Radunskaya, and Charles L Wiseman. "A validated mathematical model of cell-mediated immune response to tumor growth". In: *Cancer research* 65.17 (2005), pp. 7950–7958.

[7] Franziska Michor, Martin A Nowak, and Yoh Iwasa. "Evolution of resistance to cancer therapy". In: *Current pharmaceutical design* 12.3 (2006), pp. 261–271.

[8] Antonio Cappuccio, Filippo Castiglione, and Benedetto Piccoli. “Determination of the optimal therapeutic protocols in cancer immunotherapy”. In: *Mathematical biosciences* 209.1 (2007), pp. 1–13.

[9] E Pachepsky, RM Nisbet, and WW Murdoch. “Between discrete and continuous: consumer–resource dynamics with synchronized reproduction”. In: *Ecology* 89.1 (2008), pp. 280–288.

[10] Ignacio Ramis-Conde et al. “Modeling the influence of the E-cadherin-β-catenin pathway in cancer cell invasion: a multiscale approach”. In: *Biophysical journal* 95.1 (2008), pp. 155–165.

[11] Andrew Gelman, John Carlin, Donald Rubin, et al. *Bayesian Data Analysis (3rd ed)*. Chapman and Hall, 2013.

[12] Yangjin Kim and Soyeon Roh. “A hybrid model for cell proliferation and migration in glioblastoma”. In: *Discrete and Continuous Dynamical Systems-B* 18.4 (2013), pp. 969–1015.

[13] LG DePillis, H Savage, and AE Radunskaya. “Mathematical model of colorectal cancer with monoclonal antibody treatments”. In: *Journal of Advances in Medicine and Medical Research* 4.16 (2014), pp. 3101–3131.

[14] Hidenori Mizugaki et al. “A phase 1 study evaluating the pharmacokinetics and preliminary efficacy of veliparib (ABT-888) in combination with carboplatin/paclitaxel in Japanese subjects with non-small cell lung cancer (NSCLC)”. In: *Cancer chemotherapy and pharmacology* 76.5 (2015), pp. 1063–1072.

[15] Sheema Sameen et al. “Mathematical modeling of drug resistance due to KRAS mutation in colorectal cancer”. In: *Journal of theoretical biology* 389 (2016), pp. 263–273.

[16] Ranganatha R Somasagara et al. “Rad6 upregulation promotes stem cell-like characteristics and platinum resistance in ovarian cancer”. In: *Biochemical and biophysical research communications* 469.3 (2016), pp. 449–455.

[17] Anass Bouchnita et al. “A hybrid computation model to describe the progression of multiple myeloma and its intra-clonal heterogeneity”. In: *Computation* 5.1 (2017), p. 16.

[18] Berdine Heesterman, John-Melle Bokhorst, Jeroen Jansen, et al. “Mathematical Models for Tumor Growth and the Reduction of Overtreatment”. In: *Journal of Neurological Surgery* 80.1 (2018), pp. 72–78.

[19] Timothy Iveson et al. “3-month versus 6-month adjuvant chemotherapy for patients with high-risk stage II and III colorectal cancer: 3-year follow-up of the SCOT non-inferiority RCT”. In: *Health Technology Assessment (Winchester, England)* 23.64 (2019), p. 1.

[20] Sana Abdulkream Alharbi and Azmin Sham Rambely. “A new ODE-based model for tumor cells and immune system competition”. In: *Mathematics* 8.8 (2020), p. 1285.

[21] Heyrim Cho and Doron Levy. “The impact of competition between cancer cells and healthy cells on optimal drug delivery”. In: *Mathematical Modelling of Natural Phenomena* 15 (2020), p. 42.

[22] Glenn Ledder et al. “A discrete/continuous time resource competition model and its implications”. In: *Journal of Biological Dynamics* 15.sup1 (2021), S168–S189.

[23] Maximilian AR Strobl et al. “Spatial structure impacts adaptive therapy by shaping intra-tumoral competition”. In: *Communications medicine* 2.1 (2022), p. 46.

[24] Biao Tang et al. “A novel hybrid model of tumor control, combining pulse surveillance with tumor size-guided therapies”. In: *Applied Mathematical Modelling* 104 (2022), pp. 259–278.

[25] Oriol Abril-Pla, Virgile Andreani, Robert Zinkov, et al. “PyMC: a modern, and comprehensive probabilistic programming framework in Python”. In: *PeerJ Computer Science* 9 (2023), e1516.

[26] Anusmita Das et al. “Stability analysis of a targeted chemotherapy-cancer model”. In: *Mathematical Modelling and Control* 3.2 (2023), pp. 116–126.

[27] Rena Emond et al. “Cell facilitation promotes growth and survival under drug pressure in breast cancer”. In: *Nature Communications* 14.1 (2023), p. 3851.

[28] Jesse Kreger, Evanthia T Roussos Torres, and Adam L MacLean. “Myeloid-derived suppressor–cell dynamics control outcomes in the metastatic niche”. In: *Cancer immunology research* 11.5 (2023), pp. 614–628.

[29] Wenhui Luo, Xuewen Tan, and Juan Shen. “Optimal treatment strategy for cancer based on mathematical modeling and impulse control theory”. In: *Axioms* 12.10 (2023), p. 916.

[30] Hannah G Anderson et al. “Optimal control of combination immunotherapy for a virtual murine cohort in a glioblastoma-immune dynamics model”. In: *Journal of Theoretical Biology* 595 (2024), p. 111951.

[31] Anass Bouchnita and Vitaly Volpert. “Phenotype-structured model of intra-clonal heterogeneity and drug resistance in multiple myeloma”. In: *Journal of Theoretical Biology* 576 (2024), p. 111652.

[32] Ioannis Dassios, Angel Vaca, and Federico Milano. “On hybrid dynamical systems of differential-difference equations”. In: *Mathematical Modelling and Control* 187 (2024), p. 115431.

[33] B Krithika and P Tamilalagan. “Exploring tumor-induced immunosuppression dynamics by myeloid-derived suppressor cells: insights via a fractional-order mathematical model”. In: *The European Physical Journal Special Topics* (2024), pp. 1–18.

[34] Ryan Murphy, Oliver Maclaren, and Matthew Simpson. “Implementing measurement error models with mechanistic mathematical models in a likelihood-based framework for estimation, identifiability analysis and prediction in the life sciences”. In: *Journal of the Royal Society Interface* 21.210 (2024), p. 20230402.

[35] Boluwatife Awoyemi, Amanda Laubmeier, and Richard Rebarber. “Coexistence Fixed Points under Hybrid Timescale Dynamics with Competing Consumers”. Manuscript under review. 2025.

[36] PDQ Adult Treatment Editorial Board. “Ovarian epithelial, fallopian tube, and primary peritoneal cancer treatment (pdq®)”. In: *PDQ cancer information summaries [internet]*. National Cancer Institute (US), 2025.

[37] Kira Pugh et al. “Simulations probe the role of space in the interplay between drug-sensitive and drug-resistant cancer cells”. In: *Journal of Theoretical Biology* 602 (2025), p. 112048.

A Model Analysis

Manipulating terms form (1) and (2), we immediately conclude that

$$\begin{aligned} \frac{ST_{t+1}}{ST_t} &= \frac{(1-p)S(T^-)}{S(0)} \\ \frac{RT_{t+1}}{RT_t} &= \frac{(1-q)R(T^-)}{R(0)}. \end{aligned} \tag{6}$$

Moreover, multiplying dS/ds in (1) by $1/S$ and integrating the product from 0 to T we obtain

$$\begin{aligned} \int_0^T \frac{dS}{ds}\frac{1}{S}\,ds &= \int_0^T \left(\lambda_S - \frac{\lambda_S}{K_S}S - \frac{\lambda_S a_{SR}}{K_S}R\right) ds \\ &= \lambda_S T - \frac{\lambda_S}{K_S}\overline{S} - \frac{\lambda_S a_{SR}}{K_S}\overline{R} \end{aligned}$$

where $\overline{S} = \int_0^T S ds$ and $\overline{R} = \int_0^T R ds$. Following an identical procedure as above, for dR/ds in (1), results in a similar expression

$$\begin{aligned}\int_0^T \frac{dR}{ds}\frac{1}{R}\,ds &= \int_0^T \left(\lambda_R - \frac{\lambda_R a_{RS}}{K_R}S - \frac{\lambda_R}{K_R}R\right) ds \\ &= \lambda_R T - \frac{\lambda_R a_{RS}}{K_R}\overline{S} - \frac{\lambda_R}{K_R}\overline{R}.\end{aligned}$$

Combining the above equalities yields the following system of equations

$$\begin{aligned}\ln\left(\frac{S(T^-)}{S(0)}\right) &= \lambda_S T - \frac{\lambda_S}{K_S}\overline{S} - \frac{\lambda_S a_{SR}}{K_S}\overline{R} \\ \ln\left(\frac{R(T^-)}{R(0)}\right) &= \lambda_R T - \frac{\lambda_R a_{RS}}{K_R}\overline{S} - \frac{\lambda_R}{K_R}\overline{R}.\end{aligned} \tag{7}$$

It follows from (6) that the model described in (1) and (2) contains a positive equilibrium if and only if the following system has a positive solution.

$$\ln\left(\frac{1}{1-p}\right) = \lambda_S T - \frac{\lambda_S}{K_S}\overline{S} - \frac{\lambda_S a_{SR}}{K_S}\overline{R} \iff 0 = \lambda_S T - \ln\left(\frac{1}{1-p}\right) - \frac{\lambda_S}{K_S}\overline{S} - \frac{\lambda_S a_{SR}}{K_S}\overline{R}$$
$$\ln\left(\frac{1}{1-q}\right) = \lambda_R T - \frac{\lambda_R a_{RS}}{K_R}\overline{S} - \frac{\lambda_R}{K_R}\overline{R} \iff 0 = \lambda_R T - \ln\left(\frac{1}{1-q}\right) - \frac{\lambda_R a_{RS}}{K_R}\overline{S} - \frac{\lambda_R}{K_R}\overline{R}$$

There are observations one can make regarding the system above. The first of which is the following; suppose that the system is not linearly independent, in particular, let the second equation be a constant multiple of the first. It then follows that

$$\frac{\lambda_S}{K_S} = k\left(\frac{\lambda_R a_{RS}}{K_R}\right) \text{ and } \frac{\lambda_S a_{SR}}{K_S} = k\left(\frac{\lambda_R}{K_R}\right)$$

from which we conclude that $a_{SR}a_{RS} = 1$. An identical argument shows that $a_{SR}a_{RS} = 1$ in the case where the first equation is a constant multiple of the second. Therefore, the condition that the product $a_{SR}a_{RS}$ is equal to 1 is a necessary condition for the equations to be linearly dependent. The additional observations are contained in the subsequent theorems.

Theorem 4. *If the system of equations*

$$\begin{aligned}0 &= \lambda_S T - \ln\left(\frac{1}{1-p}\right) - \frac{\lambda_S}{K_S}\overline{S} - \frac{\lambda_S a_{SR}}{K_S}\overline{R} \\ 0 &= \lambda_R T - \ln\left(\frac{1}{1-q}\right) - \frac{\lambda_R a_{RS}}{K_R}\overline{S} - \frac{\lambda_R}{K_R}\overline{R}\end{aligned}$$

contains a positive solution, then

$$\lambda_S T - \ln\left(\frac{1}{1-p}\right) > 0 \text{ and } \lambda_R T - \ln\left(\frac{1}{1-q}\right) > 0.$$

Proof. We prove this by the contrapositive. Suppose that $\lambda_S T - \ln\left(\frac{1}{1-p}\right) \leq 0$ or $\lambda_R T - \ln\left(\frac{1}{1-q}\right) \leq 0$. Since all of the parameters in the model are assumed to be positive, if both expressions are negative, it follows that at least one of $\overline{S}$ or $\overline{R}$ is negative. Furthermore, notice that if either expression is 0, it immediately follows again that one of $\overline{S}$ or $\overline{R}$ is negative. Now, suppose that $\lambda_S T - \ln\left(\frac{1}{1-p}\right) < 0$ and $\lambda_R T - \ln\left(\frac{1}{1-q}\right) > 0$, it follows that one of $\overline{S}$ or $\overline{R}$ is 0 or negative, and thus, not positive. An identical observation can be made for the case $\lambda_R T - \ln\left(\frac{1}{1-q}\right) < 0$ and $\lambda_S T - \ln\left(\frac{1}{1-p}\right) > 0$; therefore, if either $\lambda_S T - \ln\left(\frac{1}{1-p}\right) \leq 0$ or $\lambda_R T - \ln\left(\frac{1}{1-q}\right) \leq 0$, it follows that the system does not contain a positive solution. □

A.1 Analysis of the case $a_{SR}a_{RS} = 1$

In light of the aforementioned discussion regarding a necessary condition for the linear dependence of (7), we proceed to analyze (1)-(2) in cases. We first consider the situation in which the product $a_{SR}a_{RS} = 1$, and provide a necessary condition for (1)-(2) to contain a positive equilibrium.

Theorem 5. *Suppose $a_{SR}a_{RS} = 1$, then the model has no positive equilibrium if*

$$\frac{K_R\lambda_S a_{SR}}{\lambda_R K_S}\left(\lambda_R T - \ln\left(\frac{1}{1-q}\right)\right) \neq \lambda_S T - \ln\left(\frac{1}{1-p}\right)$$

or equivalently

$$\lambda_R T - \ln\left(\frac{1}{1-q}\right) \neq \frac{\lambda_R K_S a_{RS}}{K_R\lambda_S}\left(\lambda_S T - \ln\left(\frac{1}{1-p}\right)\right).$$

Proof. Let $a_{SR}a_{RS} = 1$ and recall that the model has a positive equilibrium if and only if the following system has a positive solution

$$\begin{aligned} 0 &= \lambda_S T - \ln\left(\frac{1}{1-p}\right) - \frac{\lambda_S}{K_S}\overline{S} - \frac{\lambda_S a_{SR}}{K_S}\overline{R} \\ 0 &= \lambda_R T - \ln\left(\frac{1}{1-q}\right) - \frac{\lambda_R a_{RS}}{K_R}\overline{S} - \frac{\lambda_R}{K_R}\overline{R}. \end{aligned}$$

Multiplying the second equation by $\frac{-K_R\lambda_S a_{SR}}{\lambda_R K_S}$ we obtain

$$\begin{aligned} 0 &= \lambda_S T - \ln\left(\frac{1}{1-p}\right) - \frac{\lambda_S}{K_S}\overline{S} - \frac{\lambda_S a_{SR}}{K_S}\overline{R} \\ 0 &= -\frac{K_R\lambda_S a_{SR}}{\lambda_R K_S}\left(\lambda_R T - \ln\left(\frac{1}{1-q}\right)\right) + \frac{\lambda_S a_{RS}a_{SR}}{K_S}\overline{S} + \frac{\lambda_S a_{SR}}{K_S}\overline{R}. \end{aligned}$$

Adding the two equations together, it follows that

$$0 = \left(\lambda_S T - \ln\left(\frac{1}{1-p}\right)\right) - \frac{K_R \lambda_S a_{SR}}{\lambda_R K_S}\left(\lambda_R T - \ln\left(\frac{1}{1-q}\right)\right).$$

Hence, if

$$\frac{K_R \lambda_S a_{SR}}{\lambda_R K_S}\left(\lambda_R T - \ln\left(\frac{1}{1-q}\right)\right) \neq \lambda_S T - \ln\left(\frac{1}{1-p}\right)$$

the system has no solutions, in particular, no positive solutions. □

When system (7) exhibits linear dependence, we are able to explicitly identify a necessary condition for the existence of a positive equilibrium for (1)-(2). Establishing such a condition significantly reduces the parameter space that must be examined when one is interested in investigating the existence of positive equilibria. We also analyze the case where $a_{SR}a_{RS} \neq 1$ a provide similar results presented above.

A.2 Analysis of the case $a_{SR}a_{RS} \neq 1$

By Theorem 4 we need only take $\lambda_S T - \ln\left(\frac{1}{1-p}\right) > 0$ and $\lambda_R T - \ln\left(\frac{1}{1-q}\right) > 0$. In this case, we provide a characterization on the existence of a positive equilibrium for the model (1)-(2) for both situations where $a_{SR}a_{RS} < 1$ and $a_{SR}a_{RS} > 1$.

Theorem 6. *Let $a_{SR}a_{RS} \neq 1$. The system contains a positive equilibrium if and only if*

$$\frac{a_{RS}a_{SR}\lambda_S}{K_S}\left(\lambda_R T - \ln\left(\frac{1}{1-q}\right)\right) > \frac{a_{RS}\lambda_R}{K_R}\left(\lambda_S T - \ln\left(\frac{1}{1-p}\right)\right) > \frac{\lambda_S}{K_S}\left(\lambda_R T - \ln\left(\frac{1}{1-q}\right)\right)$$

for $a_{RS}a_{SR} > 1$, or

$$\frac{a_{RS}a_{SR}\lambda_S}{K_S}\left(\lambda_R T - \ln\left(\frac{1}{1-q}\right)\right) < \frac{a_{RS}\lambda_R}{K_R}\left(\lambda_S T - \ln\left(\frac{1}{1-p}\right)\right) < \frac{\lambda_S}{K_S}\left(\lambda_R T - \ln\left(\frac{1}{1-q}\right)\right)$$

for $a_{RS}a_{SR} < 1$.

Proof. ($\rightarrow$) Suppose there exists a positive equilibrium, then,

$$\frac{ST_{t+1}}{ST_t} = 1$$
$$\frac{RT_{t+1}}{RT_t} = 1.$$

Therefore, we have the following system of linear equations

$$\ln\left(\frac{1}{1-p}\right) = \lambda_S T - \frac{\lambda_S}{K_S}\overline{S} - \frac{\lambda_S a_{SR}}{K_S}\overline{R}$$
$$\ln\left(\frac{1}{1-q}\right) = \lambda_R T - \frac{\lambda_R a_{RS}}{K_R}\overline{S} - \frac{\lambda_R}{K_R}\overline{R}.$$

We can rewrite the system above as

$$b\overline{S} + c\overline{R} = a$$
$$g\overline{S} + f\overline{R} = d$$

where $a = \lambda_S T - \ln\left(\frac{1}{1-p}\right), d = \lambda_R T - \ln\left(\frac{1}{1-q}\right), b = \frac{\lambda_S}{K_S}, c = \frac{\lambda_S a_{SR}}{K_S}, f = \frac{\lambda_R}{K_R}$ and $g = \frac{a_{RS}\lambda_R}{K_R}$. This is a consistent system of linear equations and, hence, has a unique solution. Solving this system of equations gives

$$\overline{S} = \frac{cd - af}{cg - bf}, \quad \overline{R} = \frac{ag - bd}{cg - bf}$$

where $cg - bf \neq 0$ i.e.,

$$\frac{a_{SR}\lambda_S}{K_S}\frac{a_{RS}\lambda_R}{K_R} - \frac{\lambda_S}{K_S}\frac{\lambda_R}{K_R} \neq 0 \Longleftrightarrow (a_{SR}a_{RS} - 1)\frac{\lambda_S\lambda_R}{K_S K_R} \neq 0.$$

Since we assumed that there exists a positive equilibrium, it follows that $\overline{S}, \overline{R} > 0$. Moreover, since all of the parameters are assumed to be positive, there are two situations to consider, either $a_{SR}a_{RS} > 1$ or $a_{SR}a_{RS} < 1$. Let us first consider the case where $a_{SR}a_{RS} > 1$; in this case, $cg - bf > 0$ therefore, $cd - af > 0$ i.e.,

$$\frac{a_{SR}\lambda_S}{K_S}\left(\lambda_R T - \ln\left(\frac{1}{1-q}\right)\right) > \frac{\lambda_R}{K_R}\left(\lambda_S T - \ln\left(\frac{1}{1-p}\right)\right).$$

Similarly for $\overline{R}$, we have that $ag - bd > 0$ i.e.,

$$\frac{a_{RS}\lambda_R}{K_R}\left(\lambda_S T - \ln\left(\frac{1}{1-p}\right)\right) > \frac{\lambda_S}{K_S}\left(\lambda_R T - \ln\left(\frac{1}{1-q}\right)\right).$$

These two inequalities are equivalent to the following chain of inequalities by multiplying the inequality for $\overline{S}$ by a_{RS}

$$\frac{a_{RS}a_{SR}\lambda_S}{K_S}\left(\lambda_R T - \ln\left(\frac{1}{1-q}\right)\right) > \frac{a_{RS}\lambda_R}{K_R}\left(\lambda_S T - \ln\left(\frac{1}{1-p}\right)\right) > \frac{\lambda_S}{K_S}\left(\lambda_R T - \ln\left(\frac{1}{1-q}\right)\right).$$

An analogous argument for the case where $a_{SR}a_{RS} < 1$ shows that

$$\frac{a_{RS}a_{SR}\lambda_S}{K_S}\left(\lambda_R T - \ln\left(\frac{1}{1-q}\right)\right) < \frac{a_{RS}\lambda_R}{K_R}\left(\lambda_S T - \ln\left(\frac{1}{1-p}\right)\right) < \frac{\lambda_S}{K_S}\left(\lambda_R T - \ln\left(\frac{1}{1-q}\right)\right).$$

($\leftarrow$) Suppose first that $a_{SR}a_{RS} > 1$, and take

$$\overline{S} = \frac{cd - af}{cg - bf} > 0 \text{ and } \overline{R} = \frac{ag - bd}{cg - bf} > 0.$$

Since S and R do not change signs, and both $\overline{S} > 0$ and $\overline{R} > 0$, it follows that S and R are positive. An analogous argument holds for the case $a_{SR}a_{RS} < 1$. □

When system (7) exhibits linear independence, we again are able to explicitly identify not only a necessary condition, but also a sufficient condition for the existence of a positive equilibrium for (1)-(2). Establishing such a characterization again narrows the parameter space that must be examined when investigating the existence of positive equilibria. In both situations, $a_{SR}a_{RS} = 1$ and $a_{SR}a_{RS} \neq 1$, we were able to identify necessary conditions for the existence of positive equilibria for (1)-(2). Moreover, in the latter case, the parameter space can be further restricted by demonstrating that the necessary condition is also sufficient, thereby providing a characterization for the existence of positive equilibria.

B Hierarchical parameter inference for a cell population growth model

The logistic model equation, c.f. (3), contains three parameters: a growth rate (λ), a saturation coefficient (K) and an initial value (P_0). To determine the parameters from experimental data, we use Bayesian inference [1]. In this section, we briefly overview our Bayesian inference procedure for the interdisciplinary reader; comprehensive resources are readily available [11]. To introduce the requisite concepts, we begin with our approach to the problem of inferring the mathematical model parameters, of (3), for a single well experiment and then extend that view to the multi-well case using hierarchical inference.

B.1 Inferring model parameters for a single-well confluence experiment

At a high level, Bayesian inference can be understood as learning a probability distribution, using observed experimental data (examples shown in Figure 1), for each of the model parameters such that the resulting statistics for the data generated by our logistic model are

in good agreement with the experimental data. The foundation of Bayesian inference is Bayes' theorem

$$P(\theta \mid X) = \frac{P(X \mid \theta)P(\theta)}{P(X)}, \tag{8}$$

where θ represents the vector of model parameters, i.e. $\theta = (K, \lambda, P_0)$ in the current work, and X is the observed experimental data. In (8), $P(\theta)$ represents our prior assumptions on the parameters and $P(X \mid \theta)$ is called the likelihood and represents the probability of seeing the data X given a choice of parameters θ. Let F(t;θ) signify the logistic model, e.g. (3), with the parameters determined by a choice of $\theta = (K, \lambda, P_0)$ and let X denote the vector of observed experimental data, i.e. the confluence percentage corresponding to each time point, from a single well in a full plate experiment. To infer the posterior distributions of the parameters $\theta = (K, \lambda, P_0)$ given a single well's experimental data, we assume that the experimental data coincides with the logistic function up to some measurement noise and we use an additive Gaussian error model to determine the likelihood function [34]. This model assumes that errors are independent, additive and normally distributed; in particular, for each time t_j, the model assumes that

$$X_{t_j} - F(t_j; \theta) = \varepsilon_{t_j} \sim N(0, \sigma_E), \tag{9}$$

where X_{t_j} is the observed data at time point t_j, $F(t_j; \theta)$ is our mathematical model prediction, using the parameters θ, at time t_j, ε_{t_j} represents the sampling noise and time t_j and σ_E^2 is a variance that is the same for all time points. Thus, the distribution of X, subject to the parameter choice of θ, can be shown, using independence and that X_{t_j} is the sum of a Gaussian random variable (ε_{t_j}) and a constant ($F(t_j; \theta)$), to be

$$P(X \mid \theta) \sim N(\mu = F(t; \theta), \sigma = \sigma_E), \tag{10}$$

which we selected as our likelihood function and use in the numerator of the right-hand side of (8). For the joint prior distribution, $P(\theta) = P(K, \lambda, P_0)$ in (8), a typical assumption is that the individual parameters are independent so that

$$P(K, \lambda, P_0) = P(K)P(\lambda)P(P_0). \tag{11}$$

Though (11) may not be true in all biological models, for instance if a correlation is observed between growth rate (λ) and carrying capacity (K), it is a common assumption in practice.

Prior distributions are typically selected to be weakly informative. A weakly informative prior offers some guidance without overly constraining the search space of a Monte Carlo sampling algorithm. The guidance is typically gleaned from expert knowledge. For instance, one may select a truncated normal for $P(K)$ that reflects the fact that $0 \leq K \leq 100$. An awareness that λ is almost always experimentally approximated to be in $[0, 2]$ could be

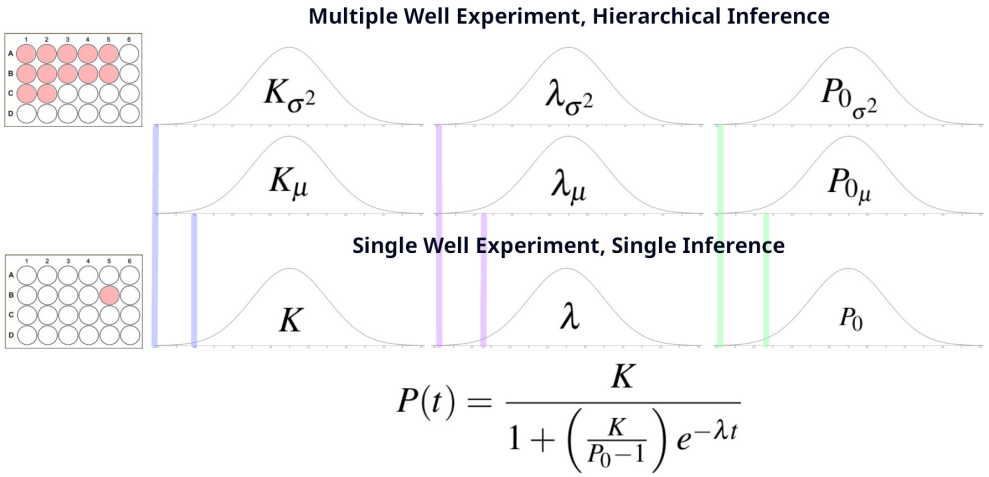

Figure 12: Bayesian inference for parameter posterior distributions; hyperparameters are shown connected with colored lines to their parent parameter. Single inference (bottom row) uses well data from one experiment to infer parameter posteriors. Hierarchical inference (top row) uses well data from multiple experiments to infer posterior distributions for hyperparameters, like the hyper-mean (K_μ) and hyper-standard deviation (K_σ), for the underlying parameter (K) distributions.

reflected by a weakly informative prior such as $P(\lambda) \sim N(0, 10)$ with a truncation to enforce a lower bound of $0 \leq \lambda$ and so forth. Following these assumptions, the likelihood (10) and individual prior densities, $P(K)$, $P(\lambda)$ and $P(P_0)$, would each then be specified in software using some statistical programming library, like PyMC [25]. PyMC, and its counterparts, allows the posterior $P(\theta \,|\, X)$ to be computed using Monte Carlo sampling algorithms, thus avoiding the need to compute $P(X)$, the problematic term to compute in (8), directly.

B.2 Inferring model parameters for a multiple-well confluence experiment

The problem of inferring the hierarchical structure of logistic well-growth dynamics can be understood as assuming that each of the parameters, governing the growth in individually observed wells, represent draws from some underlying distribution whose parameters are unknown. For instance, in a 3-well control experiment, the parameters governing the individual well growth dynamics can be written together as $\theta = (K_1, K_2, K_3, \lambda_1, \lambda_2, \lambda_3, P_{0_1}, P_{0_2}, P_{0_3})$ and the individual parameters, like K_1, K_2 and K_3, are assumed to be draws from some underlying distribution. One might assume, for illustration, that each of the K_j are draws from a normal distribution with common mean K_μ and common variance K_σ; that is

$K_j \sim N(\mu = K_\mu, \sigma = K_\sigma)$ for $j = 1,2,3$. The parameters λ_j and P_{0_j} may also follow similar assumptions. In this case, the parameters $\phi = \left(K_\mu, K_\sigma, \lambda_\mu, \lambda_\sigma, P_{0_\mu}, P_{0_\sigma}\right)$ are referred to as hyperparameters of the hierarchical model (Figure 12). The objective of the practitioner, using a hierarchical inference method, is typically to determine the set of hyperparameters, ϕ, from the experimental data though all of the parameters, in both θ and ϕ, are inferred in practice. In the hierarchical case, we may write (8) as

$$P(\theta, \phi \,|\, X) = \frac{P(X \,|\, \theta, \phi) P(\theta, \phi)}{P(X)}. \tag{12}$$

Just as in the single inference case, the Gaussian error model (9) produces the hierarchical likelihood,

$$P(X \,|\, \theta, \phi) \sim N(\mu = F(t; \theta, \phi), \sigma = \sigma_E) \tag{13}$$

where $F(t; \theta, \phi)$ denotes the outcome of the logistic model (3) pursuant to the parameters (θ) determined from a choice of hyperparameters (ϕ). Let $\theta_1 = (K_1, \ldots, K_n)$, $\theta_2 = (\lambda_1, \ldots, \lambda_n)$ and $\theta_3 = (P_{0_1}, \ldots, P_{0_n})$. In (12), $P(\theta, \phi)$ is a joint prior and a decision must be made as to its form. A common approach is factor the joint prior using the identity

$$P(\theta, \phi) = P(\theta \,|\, \phi) P(\phi), \tag{14}$$

and to make a choice as to the right-hand side terms. In our case we once again use the independence assumption for $P(\phi)$ to get

$$\begin{aligned} P(\phi) &= \prod_{i=1}^{3} P(\phi_{i,1}) P(\phi_{i,2}) \\ &= P(K_\mu) P(K_\sigma) P(\lambda_\mu) P(\lambda_\sigma) P(P_{0_\mu}) P(P_{0_\sigma}). \end{aligned} \tag{15}$$

In practice, each of the priors in (15) was implemented in PyMC as weakly informative (Table 2) and the parameter likelihood, $P(\theta \,|\, \phi)$ in (14), is determined by specifying the individual conditional distributions $P(\theta_i \,|\, \phi_{i,1}, \phi_{i,2})$ for $i = 1,2,3$ as shown in Table 2; for example, $P(K \,|\, K_\mu, K_\sigma) \sim N(\mu = K_\mu, \sigma = K_\sigma)$. PyMC then computes (14) automatically, from these individual expressions, using independence assumptions.